

Subgap states in two-dimensional spectroscopy of graphene-based superconducting hybrid junctionsOscar E. Casas,¹ Shirley Gómez Páez,^{1,2} Alfredo Levy Yeyati,³ Pablo Buset,⁴ and William J. Herrera¹¹*Departamento de Física, Universidad Nacional de Colombia, Bogotá, Colombia*²*Departamento de Física, Universidad el Bosque, Bogotá, Colombia*³*Departamento de Física Teórica de la Materia Condensada, Condensed Matter Physics Center (IFIMAC) and Instituto Nicolás Cabrera, Universidad Autónoma de Madrid, Spain*⁴*Department of Applied Physics, Aalto University, 00076 Aalto, Finland*

(Received 6 April 2018; revised manuscript received 20 July 2018; published 3 April 2019)

Several recent works have predicted that unconventional and topological superconductivity can arise in graphene, either intrinsically or by proximity effect. Then, the analysis of the spectroscopic and transport properties in graphene would be a valuable source of information in the study of the emergent superconducting order parameter. Using Green's functions techniques, we study the transport properties of a finite size ballistic graphene layer placed between a normal state electrode and a graphene lead with proximity-induced unconventional superconductivity. Our microscopic description of such a junction allows us to consider the effect of edge states in the graphene layer and the imperfect coupling to the electrodes. The tunnel conductance through the junction and the spectral density of states feature a rich interplay between graphene's edge states, interface bound states formed at the graphene-superconductor junction, Fabry-Pérot resonances originated from the finite size of the graphene layer, and the characteristic Andreev surface states of unconventional superconductors. Within our analytical formalism, we identify the separate contribution from each of these subgap states to the conductance and density of states. Our results provide an advisable tool to determine experimentally the pairing symmetry of unconventional superconductivity that can arise in graphene.

DOI: [10.1103/PhysRevB.99.144502](https://doi.org/10.1103/PhysRevB.99.144502)**I. INTRODUCTION**

Unconventional superconductivity involves all pairing states that deviate from the ordinary s -wave, spin-singlet Cooper pairs [1], and are thus classified according to the symmetry of their order parameter. For example, high- T_c superconductors feature an anisotropic d -wave spin-singlet pairing state [2,3] and there is increasing evidence for the compounds UPt_3 and Sr_2RuO_4 to be spin-triplet chiral superconductors [4]. Recently, topological superconductors [5] have triggered an intense research activity as they host gapless Majorana surface states, a candidate for fault-tolerant quantum computing [6,7]. Topological superconductivity can be artificially engineered in proximity-induced semiconductor nanowires [8–10] or naturally arises on chiral superconductors [11–13], which have a fully gapped bulk spectrum and exhibit a nonzero Chern number ($N = \pm 1$ for p wave and $N = \pm 2$ for d wave). The related chiral Andreev bound states can give rise to a rich phenomenology like spontaneous edge currents [14–16], domain walls [15], zero-energy vortices [15,17], quantized spin and thermal Hall effects [18,19], and the possibility of Majorana fermions [15,20,21]. In graphene, the peculiar hexagonal lattice allows for the formation of unconventional pairing correlations [22–27]. Indeed, it has been proposed that chiral d -wave superconductivity can arise intrinsically by doping graphene near the Van Hove singularity [23,24] or from repulsive interactions [25], whereas chiral p -wave superconductivity intrinsically appears in chemically modified, metal coated graphene [26] or by proximity to an electron-doped oxide superconductor [27]. Tunneling

conductance measurements at normal metal-superconductor junctions are a very useful tool to detect signatures of all these types of unconventional superconductivity [2]. In a ballistic junction, transport at voltages below the superconducting gap is mediated by Andreev reflections, where incident electrons are converted into holes in the normal metal creating Cooper pairs in the superconductor [28,29]. The presence of surface states in unconventional superconductors is connected to resonance peaks in the Andreev reflection probability, resulting in conductance peaks below the superconducting gap [30–35].

Unfortunately, tunneling spectroscopy of subgap resonances presents several experimental challenges, specially for nanoscale devices [29]. When considering hybrid junctions where the reservoirs and the intermediate scattering region are built from different materials, as sketched in Fig. 1(a), each interface between the intermediate region and the reservoirs may present a different transmission [36]. Additionally, quantum-coherent transport across the junction results in the emergence of Fabry-Pérot resonances [37,38]. In most of materials these effects can mask the experimental detection of novel phenomena associated to unconventional superconductivity [29]. However, recent experimental advances involving graphene-based nanoscale devices provide new ways to circumvent these challenges.

Graphene is a two-dimensional Dirac semimetal with high carrier mobility [39–41]. High-quality graphene nanoscale transistors have been achieved [42] and fabrication of graphene nanoribbons with well-defined edges is an experimental possibility [43]. Early reports of graphene-based Josephson junctions were assumed to work in the diffusive

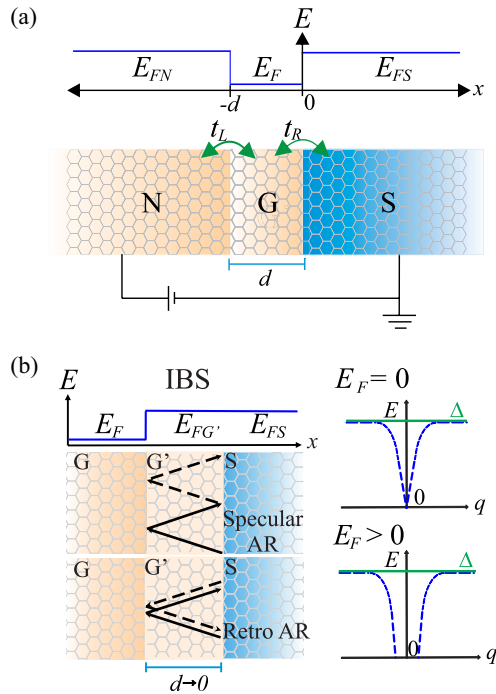


FIG. 1. Graphene N-G-S junction. (a) Schematic of the N-G-S junction, including the energy profile. (b) IBS are formed at the G-S junction and can be interpreted as standing waves located at an intermediate graphene layer G' of width $d \rightarrow 0$ (left). Sequences of Andreev specular and retro reflection processes involved in the formation of IBS are sketched: (solid) dashed arrows represent group velocities for (electron-) holelike quasiparticles. The right panel shows the dispersion relation for the IBS when the superconductor is conventional s -wave.

regime with low-transmitting interfaces [44]. Recent experiments, however, have achieved good quality ballistic graphene–superconductor contacts [45–47]. In particular, encapsulation in hexagonal boron nitride provides high-quality transparent junctions that work in the ballistic regime [46,47]. Control over the independent doping of the graphene layer has allowed to measure specular Andreev reflections [48]—an unusual type of Andreev process that only manifests when the doping is smaller than the applied voltage and the superconducting gap [49]. Advances in experimental control of graphene devices are leading to a series of remarkable works reporting spectroscopy of Andreev bound states in Josephson junctions [50], splitting of Cooper pairs [51], and possible proximity-induced superconductivity in graphene, either by growing graphene layers on superconductors [52] or by doping it with adatoms [53,54]. Graphene has been recently grown on top of unconventional (nonchiral) d -wave superconductors, revealing an interesting induced p -wave pairing state [27]. Additionally, a recent experiment reports evidence of intrinsic unconventional superconductivity in graphene superlattices [55]. More experimental and theoretical work is required to fully understand the emergent unconventional superconductivity in graphene and determine if it is chiral and topological.

In this work, we analyze the transport properties of ballistic junctions consisting of a finite graphene layer contacted by

a normal state and a superconducting macroscopic lead [cf. Fig. 1(a)]. Within our model, we study the most representative two-dimensional unconventional superconducting states that can emerge in graphene’s lattice, including nodal d -wave and chiral p - and d -wave states. Our combination of scattering and microscopic Green’s function techniques allows us to go beyond previous works in graphene-based superconducting hybrids [49,56–65] by including many of the most relevant experimental issues appearing at nanoscale graphene–superconductor junctions. Namely, by considering a finite size graphene layer we take into account the Fabry-Pérot resonances (FPR) present in experiments. Additionally, we describe imperfect coupling between the graphene layer and the reservoirs—including the effect of graphene’s zigzag edge states (ZZES)—and analyze the effect of doping the layer close or away from the Dirac point. As a result, we present differential conductance calculations with very rich subgap features, where the unconventional surface Andreev bound states (SABS) at the edge of the superconductor are mixed with FPRs, graphene’s zigzag edge states, and interface bound states (IBS) formed at the graphene–superconductor junction [63], see Fig. 1(b). We analytically describe the contribution of each process to the density of states (DOS) and differential conductance. We thus analyze the optimal conditions to detect signatures of unconventional superconductivity in graphene.

The rest of the paper is organized as follows. In Sec. II, we introduce our model and derive the main formulas for transport observables. We describe the spectral properties of G-S and N-G-S junctions in Secs. III and IV, respectively. Next, in Sec. V, we discuss the tunneling spectroscopy of unconventional superconductors. We present our conclusions in Sec. VI. The details of some of the calculations are given in Appendixes A and B.

II. MODEL

Our system consists of a graphene sheet (G) of length d and width W connected to reservoirs as sketched in Fig. 1(a). We consider transport along the x direction and assume that $W \gg d$, so that there is translational invariance along the graphene-reservoir interfaces. The left and right semi-infinite graphene contacts are in the normal (N) and superconducting (S) states, respectively. Valley degeneracy allows to describe the low-energy excitations of the coupled system by the single-valley Dirac-Bogoliubov-de Gennes (DBdG) equations $\check{H}\psi = E\psi$, with \check{H} the DBdG Hamiltonian

$$\check{H} = \begin{pmatrix} (\hat{H}_{\pm} - \varepsilon_F \hat{\sigma}_0) \hat{\sigma}_0 & \hat{\Delta} \hat{\sigma}_0 \\ \hat{\Delta}^{\dagger} \hat{\sigma}_0 & (\varepsilon_F \hat{\sigma}_0 - \hat{H}_{\pm}) \hat{\sigma}_0 \end{pmatrix}, \quad (1)$$

$\psi = (\phi_A^e, \phi_B^e, \phi_A^h, \phi_B^h)^T e^{i\mathbf{k}\cdot\mathbf{r}}$ the quasiparticle wave function in Nambu (particle-hole) and sublattice space (A and B the two triangular lattices), $E \geq 0$ the excitation energy, $\mathbf{k} = (k, q)$ the in-plane momentum vector and $\hat{\sigma}_{\nu}$ (\hat{s}_{ν}), with $\nu = 0, 1, 2$, and 3 , the Pauli matrices acting in lattice (spin) space (see Appendix A and Refs. [22,49,60,66,67] for details). The electrostatic potential of each region can be independently fixed and we take $\varepsilon_F = E_{FN}$, E_F , and E_{FS} for regions N, G, and S, respectively. In the Hamiltonian (1), the pair potential is proportional to the identity matrix in lattice space $\hat{\sigma}_0$, and couples electrons and holes in the same sublattice from

different valleys [22,49,60,61,66–69]. For each valley, we use the Dirac Hamiltonian $\hat{H}_\pm = -iv_F\partial_x\hat{\sigma}_1 \pm v_Fq\hat{\sigma}_2$, with v_F the Fermi velocity and q the conserved component of the wave vector parallel to the interfaces. Since the DBdG equations for each valley contain the same dynamics and are related by time reversal operation, we initially describe \hat{H}_+ only and later we discuss the role of the other valley.

In the vicinity of the Dirac point for the weak-coupling approximation, the superconducting order parameter depends only on the momentum direction [22,60] and is only nonzero in region S, i.e., $\hat{\Delta}(\theta, x) = \hat{\Delta}(\theta)\Theta(x)$, with $\Theta(x)$ the Heaviside function, $\theta = \sin^{-1}(q/k_{FS})$ the angle in reciprocal space and k_{FS} the Fermi wave vector. We only consider spin-degenerate unconventional superconductors which allows us to decouple the spin degree of freedom in Eq. (1) [1,33,70]. Indeed, for spin-singlet states, we have $\hat{\Delta}(\theta) = \Delta(\theta)e^{i\phi}(i\hat{s}_2)$, with ϕ the global U(1) gauge phase. Analogously, for spin-triplet superconductors we take $\hat{\Delta}(\theta) = e^{i\phi}\mathbf{d}(\theta) \cdot \hat{\mathbf{s}}(i\hat{s}_2)$, with the odd vector function $\mathbf{d}(\theta) = -\mathbf{d}(\pi - \theta)$. As long as the vector \mathbf{d} is perpendicular ($\mathbf{d} \propto \hat{\mathbf{z}}$) or parallel to the x - y graphene plane, the spin degree of freedom can be decoupled in Eq. (1).

Under these approximations, the resulting DBdG equations read as

$$\begin{pmatrix} v_F\mathbf{k}_\alpha \cdot \hat{\sigma} - \varepsilon_F\hat{\sigma}_0 & \Delta(\theta_\alpha)e^{i\phi}\hat{\sigma}_0 \\ \Delta^*(\theta_\alpha)e^{-i\phi}\hat{\sigma}_0 & \varepsilon_F\hat{\sigma}_0 - v_F\mathbf{k}_\alpha \cdot \hat{\sigma} \end{pmatrix} \begin{pmatrix} \phi_\alpha^e \\ \phi_\alpha^h \end{pmatrix} = E \begin{pmatrix} \phi_\alpha^e \\ \phi_\alpha^h \end{pmatrix}, \quad (2)$$

with $\alpha = \pm$ for right and left movers, respectively. We notice here that, since the lattice is acting as a pseudospin degree of freedom, the reduced Hamiltonian of Eq. (2) is also suitable to describe induced pairing amplitudes with an structure in lattice space [22,26,27,67,71], with the appropriate redefinition of the pair potential. More details about Eq. (2) and its solutions can be found in Appendix A.

To take into account the sign change of the triplet state with the wave vector, we only consider $k_x \geq 0$ and define $\mathbf{k}_\alpha = (\alpha k_x, q)$. We thus set $\theta_+ = \theta$ and $\theta_- = \pi - \theta$ for right and left movers, respectively. We adopt the following form for the order parameter [35,72,73]

$$\Delta(\theta_\pm) = \Delta_0[r_1 \cos(n\theta_\pm) + ir_2 \sin(n\theta_\pm)], \quad (3)$$

with $\Delta_0 \geq 0$ the potential amplitude, and $r_1, r_2 = \sqrt{1 - r_1^2}$ the relative weights of the real and imaginary parts of the pair potential. The integer $n = 0, 1, 2, \dots$ determines the orbital symmetry of the pairing state, i.e., the values $n = 0, 2$ correspond s - and d -wave states, respectively, while $n = 1$ represents a p -wave state.

The retarded/advanced Green functions associated to the Hamiltonian in Eq. (2) satisfy the nonhomogeneous DBdG equation

$$[\check{H} - (E \pm i0^+)\check{I}]\check{g}_q^{r,a}(x, x') = \delta(x - x')\check{I}, \quad (4)$$

where $\check{g}_q^{r,a}(x, x')$ is the Fourier transform of the spatial Green function on the coordinates parallel to the interfaces, \check{I} is the four-dimensional identity matrix and \check{H} is given by Eq. (2) in real space ($\hbar k_x \rightarrow -i\hbar\partial_x$). The unperturbed Green's function $\check{g}_q^{r,a}(x, x')$ is obtained combining asymptotic solutions that obey boundary conditions at the edges of a finite length graphene sheet, following a generalization of the method

developed in Refs. [2,68,74–78] for unconventional superconductors and described in Appendix B).

Once the Green functions for the isolated finite graphene layers have been obtained, the Green functions of the coupled system \check{G} are calculated by means of an algebraic Dyson equation of the form [68,79]

$$\check{G}_{q,ij}^{r,a} = \check{g}_{q,ij}^{r,a} + \check{g}_{q,ik}^{r,a}\hat{t}_{kl}\check{G}_{q,lj}^{r,a}, \quad (5)$$

with short-hand notation $\check{g}_{q,ij}^{r,a} = \check{g}^{r,a}(x_i, x'_j, E, q)$. Since the expression for Green functions with zigzag edges depends on the order of spatial arguments [68,79], it is necessary to keep an infinitesimal distance between spatial arguments in order to define ‘‘local’’ Green functions. The hopping matrix \hat{t}_{kl} ($k \neq l$) couples two different regions and depends on the type of edges between these [68]. For the zigzag boundary conditions adopted in this work, opposite edges of the graphene layer correspond to atoms from a different sublattice and the wave functions have null A (B) components at the right (left) edges. This leads to a specific form of the hopping matrix as defined below.

Transport observables

The spectral density of states is calculated from the retarded Green function as

$$\mathcal{A}(x, E, q) = -\frac{1}{\pi} \text{Im} \{ \text{Tr} \check{G}_{ee}^r(x, x, E, q) \}, \quad (6)$$

where the trace is taken over the electron-electron component in Nambu space. The local density of states (DOS) is given by

$$\rho(x, E) = \int dq \mathcal{A}(x, E, q). \quad (7)$$

The current for a setup with three regions L, C, R [like the one sketched in Fig. 1(a) for regions G, G', S] is obtained following the Hamiltonian approach [79,80]. To do so, we define the total Hamiltonian

$$\hat{H}(\tau) = \hat{H}_L + \hat{H}_C + \hat{H}_R + \hat{H}_{TL}(\tau) + \hat{H}_{TR}(\tau), \quad (8)$$

where $\hat{H}_{L,C,R}$ are the unperturbed Hamiltonians for the left (L), central (C) and right (R) regions, given by Eq. (1) evaluated with the appropriate parameters described in the next sections (e.g., $\Delta = 0$ for L and C and so forth). Each region is also described by an unperturbed Green function obtained from Eq. (4). $\hat{H}_{TL,R}(\tau)$ are the tunneling Hamiltonians between the central and the exterior regions, namely,

$$\hat{H}_{TL}(\tau) = \sum_\sigma \int dq t_L e^{i\phi_L(\tau)/2} \hat{c}_{q,LB\sigma}^\dagger \hat{b}_{q,LA\sigma} + \text{H.c.}, \quad (9)$$

$$\hat{H}_{TR}(\tau) = \sum_\sigma \int dq t_R e^{i\phi_R(\tau)/2} \hat{c}_{q,RA\sigma}^\dagger \hat{b}_{q,RB\sigma} + \text{H.c.}, \quad (10)$$

where $t_{L(R)}$ are the left and right hopping amplitudes, $\phi_{L(R)}(\tau) = \phi_0 + 2(\mu_{L(R)} - \mu_C)\tau/\hbar$ are the time-dependent gauge phase induced by the difference of chemical potentials at the interfaces, $\hat{c}_{q,vj\sigma}$, with $v = L, R$ and $j = A, B$, are annihilation operators for electrons at the edges of the L and R regions with parallel momentum q and spin σ , and $\hat{b}_{q,vj\sigma}$ are the analogous annihilation operators for the L and R edges of the central region. We assume that the central region C is

terminated by zigzag edges formed by atoms from sublattice A (B) on the right (left) side. The average current through the left interface is given by

$$\begin{aligned} I(\tau) &= -e \left\langle \frac{d}{d\tau} \hat{N}_L(\tau) \right\rangle \\ &= \frac{ie}{\hbar} \sum_{\sigma} \int dq \{ t_L [\hat{c}_{q,LB\sigma}^{\dagger}(\tau) \hat{b}_{q,LA\sigma}(\tau) \\ &\quad - t_L^{\dagger} \langle \hat{b}_{q,LA\sigma}^{\dagger}(\tau) \hat{c}_{q,LB\sigma}(\tau) \rangle] \}. \end{aligned} \quad (11)$$

This average can be expressed in terms of the Keldysh or nonequilibrium Green functions defined as [79,80]

$$\hat{G}_{q,ij}^{\alpha\beta}(\tau_{\alpha}, \tau'_{\beta}) = -i \langle \hat{T} [\hat{D}_{q,i}(\tau_{\alpha}) \hat{D}_{q,j}^{\dagger}(\tau'_{\beta})] \rangle, \quad (12)$$

where superscripts α, β correspond to the temporal branches of the Keldysh contour, \hat{T} is the Keldysh time-ordering operator and

$$\hat{D}_{q,i}^{\dagger}(\tau) = (\hat{d}_{q,iA\uparrow}^{\dagger}(\tau), \hat{d}_{q,iB\uparrow}^{\dagger}(\tau), \hat{d}_{q,iA\downarrow}(\tau), \hat{d}_{q,iB\downarrow}(\tau)),$$

$i, j = L, C, C', R$ label the edges and are defined according to the relations $\hat{d}_{q,Lj\sigma}(\tau) = \hat{c}_{q,Lj\sigma}(\tau)$, $\hat{d}_{q,Cj\sigma}(\tau) = \hat{b}_{q,Lj\sigma}(\tau)$, $\hat{d}_{q,C'j\sigma}(\tau) = \hat{b}_{q,Rj\sigma}(\tau)$, $\hat{d}_{q,Rj\sigma}(\tau) = \hat{c}_{q,Rj\sigma}(\tau)$. Here, C and C' correspond to the leftmost and rightmost edges of the central region, respectively. Then, the average current takes the form

$$I(\tau) = \frac{e}{\hbar} \int dq \text{Tr} \{ \check{\tau}_z [\check{t}_L \check{G}_{q,CL}^{+-}(\tau, \tau) - \check{t}_L^{\dagger} \check{G}_{q,LC}^{+-}(\tau, \tau)] \},$$

where $\check{\tau}_z$ is the z Pauli matrix in Nambu space and $\check{t}_{L(R)} = (t_{L(R)}/2) \check{\tau}_z (\hat{\sigma}_x - i\hat{\sigma}_y)$ are the hopping matrices associated to Eqs. (9) and (10). Since we are studying a stationary situation, the Green functions would depend only on the difference of temporal arguments. Then, by taking the Fourier transform of Green functions to energy space, we have

$$I = \frac{e}{\hbar} \int dq \frac{dE}{2\pi} \text{Tr} \{ \check{\tau}_z [\check{t}_L \check{G}_{q,CL}^{+-}(E) - \check{t}_L^{\dagger} \check{G}_{q,LC}^{+-}(E)] \}.$$

Using the properties of the nonequilibrium Green functions, the last expression can be written in terms of local nonequilibrium Green functions

$$I = \frac{e}{\hbar} \int dq dE \text{Tr} \{ \check{\tau}_z \check{t}_L^{\dagger} [\check{g}_{q,LL}^{+-} \check{t}_L \check{G}_{q,CC}^{+-} - \check{g}_{q,LL}^{+-} \check{t}_L \check{G}_{q,CC}^{+-}] \}, \quad (13)$$

where $\check{g}_{q,ii}^{+-} = 2\pi i \check{\rho}_{q,i} f_i$ and $\check{g}_{ii}^{-+} = -2\pi i \check{\rho}_{q,i} (\hat{\tau}_0 \hat{\sigma}_0 - \check{f}_i)$ are the nonequilibrium Green functions for the uncoupled electrodes evaluated at the edges, with $\check{\rho}_{q,i} = \mp \text{Im}(\check{g}_{q,ii}^{(a)})/\pi$ the related local density of states matrix, and \check{f}_i the Fermi-Dirac distribution matrix of electrode i for an applied voltage $V_i = (\mu_i - \mu_C)/e$, defined as $\check{f}_i(E, V_i) = \text{diag}(f(E - eV_i)\hat{\sigma}_0, f(E + eV_i)\hat{\sigma}_0)$ with $f(E) = [1 + \exp(\beta E)]^{-1}$ and β the inverse temperature (we have adopted the limit $T \rightarrow 0$ and for simplicity of notation the E dependence of the Green functions has been omitted). The coupled nonequilibrium Green functions can be written in terms of the retarded/advanced Green functions by means of the following Dyson equation:

$$\check{G}_{q,CC}^{\gamma} = \check{G}_{q,CC}^r \check{t}_L^{\dagger} \check{g}_{q,LL}^{\gamma} \check{t}_L \check{G}_{q,CC}^a + \check{G}_{q,CC}^r \check{t}_R \check{g}_{q,R}^{\gamma} \check{t}_R^{\dagger} \check{G}_{q,C,C}^a, \quad (14)$$

where $\gamma = +- , -+$ are Keldysh contour indexes. Finally,

$$\begin{aligned} I &= \frac{4\pi^2 e}{h} \int dq dE \text{Tr} \{ \check{\tau}_z \check{t}_L^{\dagger} \check{\rho}_{q,L} \\ &\quad \times ([\check{f}_L \check{t}_L \check{G}_{q,CC}^r \check{t}_L^{\dagger} \check{\rho}_{q,L} - \check{t}_L \check{G}_{q,CC}^r \check{t}_L^{\dagger} \check{\rho}_{q,L} \check{f}_L] \check{t}_L \check{G}_{q,CC}^a \\ &\quad + [\check{f}_L \check{t}_L \check{G}_{q,CC}^r \check{t}_R \check{\rho}_{q,R} - \check{t}_L \check{G}_{q,CC}^r \check{t}_R \check{\rho}_{q,R} \check{f}_L] \check{t}_R^{\dagger} \check{G}_{q,C,C}^a \}. \end{aligned}$$

The differential conductance at zero temperature reads [79] ($V = V_L - V_R$)

$$\sigma(V) = \frac{\partial I}{\partial V} = \sigma_A + \sigma_Q, \quad (15)$$

where σ_A is the contribution of Andreev processes,

$$\sigma_A = \int dq \frac{16e^2}{h} \text{Tr} \{ \text{Re} \{ \bar{\rho}_{q,Lee} \hat{G}_{q,CCeh}^r \bar{\rho}_{q,Lhh} \hat{G}_{q,CChe}^a \} \}, \quad (16)$$

with $\bar{\rho}_{q,L\mu\nu}$ the Nambu components of the matrix $\bar{\rho}_{q,L} = \pi \check{t}_L^{\dagger} \check{\rho}_{q,L} \check{t}_L$. The contribution due to quasiparticles is given by

$$\begin{aligned} \sigma_Q &= \int dq \frac{8e^2}{h} \text{Tr} \{ \text{Re} \{ \bar{\rho}_{q,Lee} \\ &\quad \times (\hat{G}_{q,CC'ee}^r [\bar{\rho}_{q,Ree} \hat{G}_{q,C'Cee}^a - \bar{\rho}_{q,Reh} \hat{G}_{q,C'Che}^a] \\ &\quad - \hat{G}_{q,CC'eh}^r [\bar{\rho}_{q,Rhe} \hat{G}_{q,C'Cee}^a - \bar{\rho}_{q,Rhh} \hat{G}_{q,C'Che}^a]) \} \}, \end{aligned} \quad (17)$$

where $\bar{\rho}_{q,R\mu\nu}$ are the Nambu components of $\bar{\rho}_{q,R} = \pi \check{t}_R \check{\rho}_{q,R} \check{t}_R^{\dagger}$. We use a highly doped semi-infinite graphene lead in order to model the normal electrode. Conductances are normalized to the normal-state graphene conductance. Equation (15) provides a generalized formula to calculate the differential conductance in graphene-superconductor hybrid structures.

III. SPECTRAL PROPERTIES OF GRAPHENE-SUPERCONDUCTOR JUNCTIONS

The spectral properties of the full N-G-S system contain information from many different sources: ZZES, FPR, IBS, and SABS. We analyze the N-G-S setup numerically in the next section. In some particular cases, however, we can obtain simple analytical formulas for the contribution from some of these states. In this section, we consider a simpler setup where the left electrode is removed, resulting in a graphene-superconductor (G-S) junction, where we have taken the highly doped limit for the superconductor region, see Fig. 1(b). The coupled Green function is given by Dyson's equation introduced in Eq. (5) (see Appendix B for more details). The denominator of this perturbed Green function encodes information about the different states present in the junction. By finding its zeros, we obtain the dispersion relation of the induced resonances in the junction. In this section, we assume a perfect coupling between the graphene layer and the superconductor to avoid the formation of ZZES at the G-S interface. However, for finite graphene layers, there is another ZZES at the opposite edge. Analyzing the Green function at the G-S interface, we can minimize the impact of ZZES on the spectrum and focus on the other resonances.

First, a N-S interface with an unconventional superconductor always manifests with the emergence of SABS with a dispersion relation given by [81]

$$E_{\text{SABS}} = \pm |\Delta(\theta)| \cos \Delta\varphi/2, \quad (18)$$

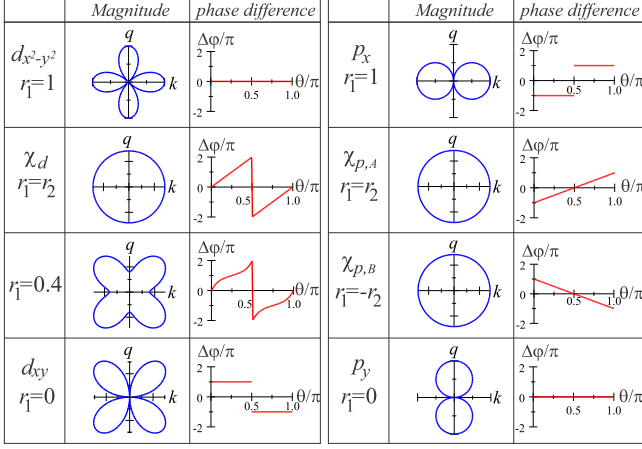


FIG. 2. Order parameter and angle dependence of the phase difference between pair potentials, given in Eq. (18), for the d -wave and p -wave symmetries considered. See text for more details.

with $\Delta\varphi = \varphi_+ - \varphi_-$ the phase difference between the pair potentials $\Delta(\theta_+)$ and $\Delta(\theta_-)$ defined in Eq. (3). Eq. (18) takes different forms depending on the symmetry of the pair potential, cf. Fig. 2. For symmetries s , $d_{x^2-y^2}$ and p_y ($\Delta\varphi = 0$), we get $E = \pm|\Delta(\theta)|$. For d_{xy} and p_x symmetries, we have $\Delta\varphi = \pi$ which corresponds to zero energy states $E = 0$. Chiral symmetries feature an angle dependence as follows: chiral d -wave symmetry χ_d ($\Delta\varphi = 4\theta$) results in $E = \pm|\Delta(\theta)|\cos 2\theta$, and chiral p -wave χ_p ($\Delta\varphi = \text{sgn}(r_1)2\theta + \pi$) gives $E = \pm|\Delta(\theta)|\sin\theta$. However, the chirality feature requires a full analysis of the numerator of the coupled Green function [see the last expression in Appendix B]. The spectral density of states in Figs. 3(b) and 3(h) shows the two topological co-propagating chiral modes associated to the Chern number $N = 2$ for chiral d -wave symmetries, while in Figs. 3(e) and 3(k) the unique chiral p -wave state corresponding to $N = 1$ can be appreciated [23,24].

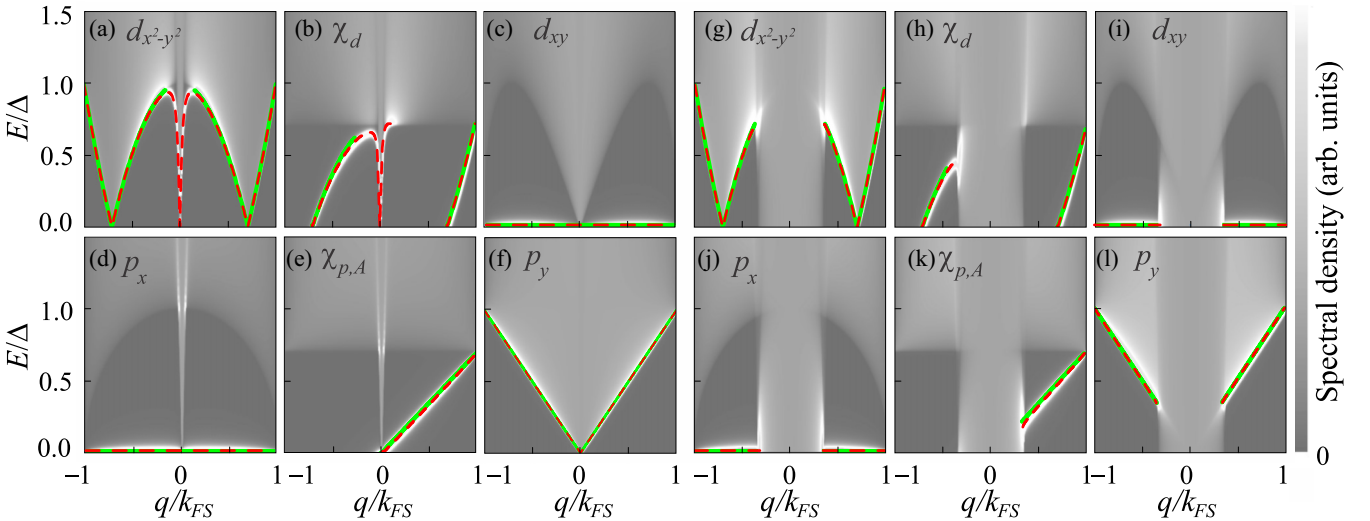


FIG. 3. Spectral density of states of a semi-infinite graphene sheet coupled to a semi-infinite anisotropic superconductor evaluated at the interface. $E_F = 0$ in (a)–(f) and $E_F = 10\Delta$ in (g)–(l). SABS (solid green lines) and IBS (dashed red lines) are depicted for the different symmetries.

In addition to the SABS, the special properties of the graphene layer lead to the emergence of IBS [63], describing how the linear dispersion of graphene adapts to the presence of the gapped superconducting density of states [see Fig. 1(b)]. Moreover, a finite graphene layer will feature ZZES and discrete energy bands, labeled here FPR. A general expression that describes IBS and FPR reads as

$$E_{G-S} = \pm \left(\frac{C \cos(\Delta\varphi/2) + i \sin(\Delta\varphi/2)}{\sqrt{C^2 - 1}} \right) |\Delta(\theta)|, \quad (19)$$

with

$$C = \frac{1 + e^{-i\alpha_e} e^{i\alpha_h} h_+ h_-}{e^{-i\alpha_e} h_+ + e^{i\alpha_h} h_-}, \quad h_{\pm} = \frac{e^{\pm 2idk_e(h)} - 1}{e^{\mp 2i\alpha_e(h)} e^{\pm 2idk_e(h)} + 1}.$$

Here, $e^{i\alpha_e(h)}$ is associated with the angle of incidence of quasi-particles in the graphene region and is defined in Appendix B. For s -wave Eq. (19) coincides with the results in Ref. [63]. For this symmetry, the dispersion relation of the IBS tends to zero at $q \rightarrow 0$ and approaches asymptotically the superconducting gap for large q as it is sketched in Fig. 1(b). The IBS are localized at the G-S interface for $E_F \gg \Delta$ (retroreflection regime) but can decay over long distances inside the graphene region when $E_F \ll \Delta$ (specular reflection regime). We now consider two specific cases where Eq. (19) can be simplified to isolate the contribution from either IBS or FPR (both in the presence of SABS).

A. Low-doped semi-infinite graphene layer: interface bound states

By considering now a semi-infinite graphene layer coupled to a superconductor, we can ignore the geometrical FPR and ZZES and focus on the dispersion relation corresponding to the SABS and IBS. By coupling transparently the semi-infinite graphene Green function to the superconducting electrode, we obtain a dispersion relation for the IBS that

corresponds to taking the limit $d \rightarrow \infty$ in Eq. (19), where $h_{\pm} \rightarrow -1$. In the heavily doped regime with $E_F \gg E$, Δ , the dispersion relation is given by Eq. (18)—the IBSs only appear for low doping levels comparable to the superconducting gap.

At the opposite limit, i.e., close to the Dirac point, $E_F = 0$, we find that Eq. (19) yields

$$E_{\text{IBS}} \approx \pm \varepsilon |\Delta(\theta)| \sqrt{\frac{(1 - \eta^2)(\varepsilon^2 + |\Delta(\theta)|^2)}{\varepsilon^4 + |\Delta(\theta)|^4 - 2\varepsilon^2 |\Delta(\theta)|^2 (2\eta^2 - 1)}}, \quad (20)$$

with $\varepsilon = \hbar v_F q$ and $\eta = \sin(\Delta\varphi/2)$.

We show the spectral density of states, Eq. (6), for a semi-infinite graphene layer coupled to a superconductor in Fig. 3. We evaluate Eq. (6) at the graphene-superconductor interface and consider different pairing symmetries according to Fig. 2. All results are evaluated for one of graphene's valleys and can show an asymmetry in the momentum $\hbar q$. This asymmetry is explained in detail in the next section. The continuous band is shown in gray, with the subgap resonances appearing in bright over the dark background of the superconducting gap. The resonances have been fitted using the formulas derived in this section, solid green lines for SABS [Eq. (18)] and dashed red lines for IBS [Eq. (20) for $E_F = 0$ and Eq. (19) for $E_F \neq 0$, which reduces practically to Eq. (18) in the heavily doped regime]. The close similarity between red and green lines demonstrates how SABS and IBS are connected in the semi-infinite layer. This setup corresponds to an ideal case where induced pairing in graphene is mostly given by the unconventional pair amplitude in the superconductor, without spurious effects from FPR or ZZES. Indeed, for symmetries s , $d_{x^2-y^2}$, and p_y , the dispersion relation in Eq. (20) reduces to $E = \pm \varepsilon |\Delta(\theta)| [\varepsilon^2 + |\Delta(\theta)|^2]^{-1/2}$ as can be seen in Fig. 1(b) (for s -wave symmetry) and in the red dashed plot of Figs. 3(a) and 3(f). For d_{xy} and p_x symmetries, Eq. (20) features a ZES, see Figs. 3(c) and 3(d). For chiral symmetries, $\eta = \text{sgn}(r_1) \sin(\Delta\varphi/2)$ and $|\Delta(\theta)| = \Delta/\sqrt{2}$ in Eq. (20) [Figs. 3(b) and 3(e)].

B. Heavily doped finite graphene layer: Fabry-Pérot resonances

A finite graphene layer develops FPR and ZZES. By taking the heavily doped limit, we get rid of the effect of both ZZES and IBS, leaving only the interplay between the geometric FPR and the proximity-induced SABS. The dispersion relation Eq. (19) takes the simple form

$$E_{\text{FPR}} = \pm |\Delta(\theta)| \cos \left((k_e - k_h)d - \frac{\Delta\varphi}{2} \right). \quad (21)$$

where k_e and k_h are defined in Appendix B). Following Ref. [81], we approximate $k_e - k_h \simeq 2E/\hbar v_F$ to obtain

$$E = \frac{\hbar v_F}{2d} \left(\pm 2\pi n + \frac{\Delta\varphi}{2} + \cos^{-1}(\pm E/|\Delta(\theta)|) \right). \quad (22)$$

Note that the separation between energy levels decreases with the length d of the stripe and, therefore, the number of levels per unit of energy—and thus the number of conductance peaks—increases with d . Eq. (21) can be interpreted as the intersection points between a straight line with slope $|\Delta(\theta)|^{-1}$ and a harmonic function with frequency $2d/\hbar v_F$ and phase

$\Delta\varphi/2$. For pairing symmetries with a dependence on the angle of incidence θ , as $\Delta\varphi$ continuously changes from 0 to π , the harmonic function in Eq. (21) shifts from $\cos x$ to $\sin x$ and the intersection points approach to $E = 0$. This induces a gradual shifting of the crests to the center and finally the emergence of a ZES state. As a result, there is a shifting of resonance peaks in the differential conductance σ until the appearance of a ZBCP (more details in Sec. V).

IV. DENSITY OF STATES OF THE N-G-S JUNCTION

We now focus on the N-G-S junction sketched in Fig. 1(a). The intermediate region is a graphene layer with zigzag edges along the y direction. When uncoupled from the reservoirs, the isolated graphene layer features localized zigzag edge states (ZZES) at $E = -E_F$. The coupling to the leads, controlled by the interface transparencies $t_{L,R}$, splits the ZZES which completely vanish at perfect transparency [58,63,68,82–84]. The ZZES have a resonant contribution to the density of states, with magnitude much bigger than that of any other resonances or Andreev states considered here. They thus play an important role in the tunneling properties, as shown in the next section. In what follows, we take $t_L = 0.1$ and $t_R = 1$. A perfect coupling to the superconductor ($t_R = 1$) guarantees that at the interface there is no ZZES and only Andreev reflections take place. By considering the coupling to the N lead in the tunnel regime ($t_L = 0.1$), we include an important contribution from normal backscattering processes and from the ZZES at that edge. We choose the width of the graphene layer to be $d = 2\xi$, with $\xi = \hbar v_F/\Delta$ the superconducting coherence length. This is enough for Andreev processes to contribute to the conductance to the leftmost electrode, but it also reduces the effect of the ZZES on the density of states calculated close to the G-S interface. Additionally, the reduced N-G tunneling increases the finite-size effects at the intermediate region.

Under such conditions, we plot in Fig. 4 the spectral density and DOS, calculated, respectively, from Eqs. (6) and (7) close to the G-S interface ($x \rightarrow 0$), for the d -wave symmetries. An equivalent plot for p -wave symmetries is shown in Fig. 5. Before analyzing the effect of the different pairing symmetries, we first comment on some common effects stemming from the band structure of the finite graphene layer.

The asymmetry of the bands with respect to the wave vector is better explained in Fig. 6 using chiral p -wave symmetry. The results in Figs. 4 and 5 are calculated for one of the valleys. For the other valley, the pair potential is also given by Eq. (3) but with the change $q \rightarrow -q$. As a consequence, the asymmetric FPR bands inside the Dirac cone are reflected in the q axis for the other valley. The symmetry with respect to the energy in the DOS is thus recovered when the contribution from both valleys is considered together, see Fig. 6(c). The change of valley does not affect the dispersion relation of the IBS and SABS for chiral symmetries, and chirality is preserved in the total contribution of the spectral density, as it is shown in Fig. 6.

The finite size is manifested by the appearance of discrete bands instead of a continuous spectrum like in Fig. 3. For the undoped cases with $E_F = 0$, e.g., Figs. 4(a)–4(d), a band appears inside the gap at the Dirac point. A second band

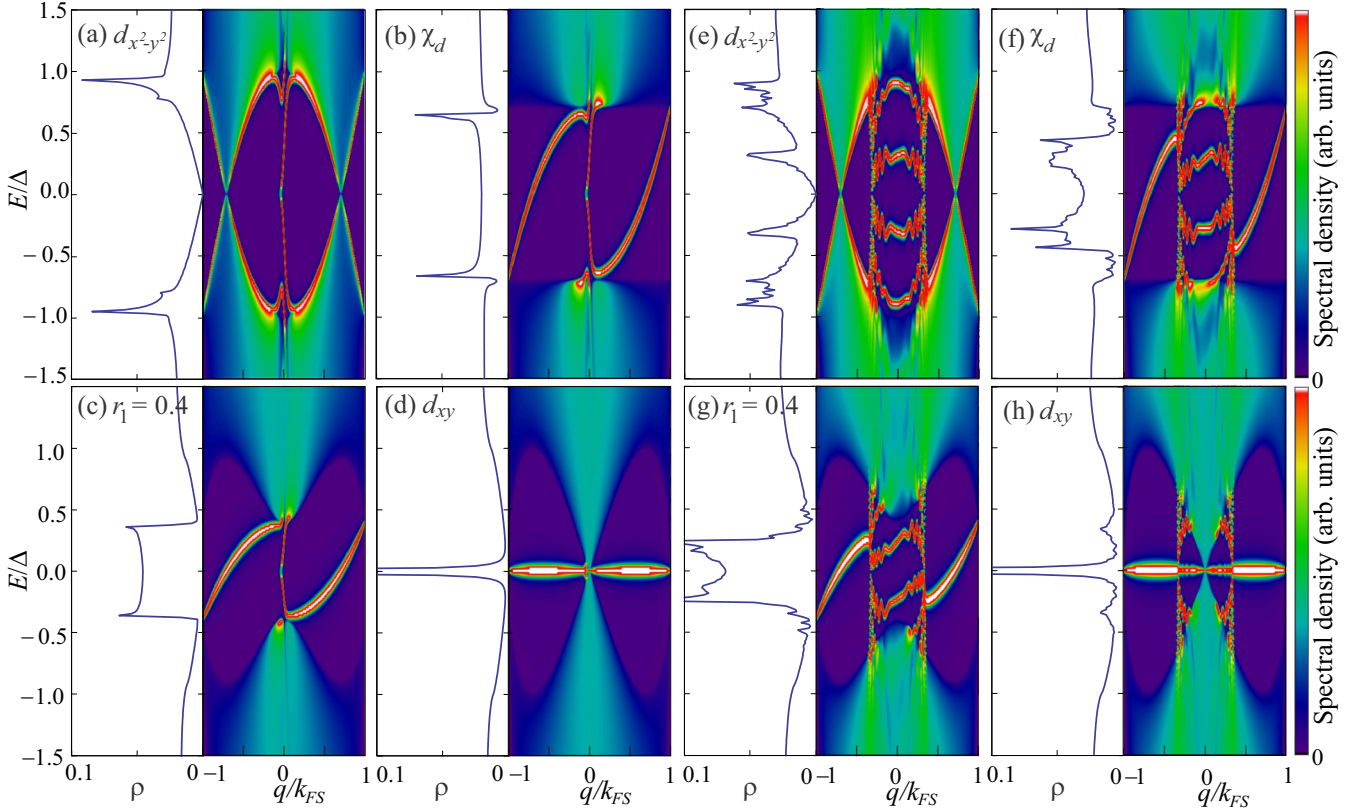


FIG. 4. Spectral density and DOS of the graphene N-G-S junction at $x = 0$. Results for d -wave superconductors with different values of the pairing phase. The Fermi energy of the graphene layer is $E_F = 0\Delta$ in (a)–(d) and $E_F = 10\Delta$ in (e)–(h). In all cases, $E_{FN} = E_{FS} = 30\Delta$, $t_L = 0.1$, $t_R = 1$, and $d = 2\xi$.

can be perceived close to the gap edge, for the symmetries with a full gap around $q \sim 0$, like $d_{x^2-y^2}$ in Fig. 4(a) and p_x in Fig. 5(a). To better analyze the FPR, we consider a heavily doped regime with $E_F = 10\Delta$ in Figs. 4(e)–4(h) and 5(e)–5(h). The extra bands emerging from high doping appear as wavy arc-shaped bands framed by the anisotropic superconducting gap and no ZZES band is present as predicted by Eq. (21).

We now focus on the effect of an unconventional pairing induced in graphene. For the $d_{x^2-y^2}$ -wave symmetry, graphene's band structure is deformed according to the $\cos 2\theta$ dependence of the pairing amplitude, cf. Fig. 4(a). As a result, the DOS features a V -shaped gapped profile, even in the presence of FPR, see Fig. 4(e). Even after adding up all the momentum channels in the DOS, we can still observe in the left panel of Fig. 4(a) a small contribution from the layer's second band as a small peak below the gap edge. For d_{xy} -wave symmetry, where the gap edge now follows a $\sin 2\theta$ dependence, there is a clear zero-energy peak in the DOS coming from the emergence of a flat band in the spectrum, see Figs. 4(d) and 4(h). The intermediate instance between these symmetries is well represented by the chiral case with $r_1 = 0.4$, Figs. 4(c) and 4(g), where the flat band acquires a dispersion for the chiral topological SABS at the same time that the gap edge is deformed similarly to the d_{xy} -wave case. The DOS captures such a superposition of d -wave states displaying a smaller effective gap region with increased DOS due to the presence of the chiral states but still featuring the increased DOS in

the gap region and a minimum at zero energy. The FPR can now mask this effect in the DOS, cf. Fig. 4(g), but the local minimum at $E = 0$ remains. The situation where both $d_{x^2-y^2}$ and d_{xy} weight exactly the same in the pairing states is the chiral d -wave (χ_d) case, shown in Figs. 4(b) and 4(f). For this chiral symmetry the effect of the topological chiral SABS is better perceived: the DOS is finite but features a U -shaped gap profile with sharp edges and the chiral SABS crossing the gap is clearly visible in the spectral density.

For p -wave symmetries, we find analogous results with some important differences. Similarly to the d_{xy} -wave case, p_x -wave symmetry features a zero-energy peak in the DOS from a flat band, independently of the doping level, see Figs. 5(a) and 5(e). Analogously, p_y -wave symmetry features a V -shaped DOS comparable to that of $d_{x^2-y^2}$ wave, as shown in Figs. 5(d) and 5(h). It is important to notice that for p_y wave there are two nodes instead of the resonances at $E = \pm\Delta$, a characteristic feature of p -wave superconductors. In the presence of disorder, d_{xy} and p_x waves (and, correspondingly, $d_{x^2-y^2}$ and p_y waves) display different behavior and can be thus distinguished better [34,35].

The chiral p -wave symmetry, χ_p , shows an interesting difference with respect to the χ_d case. The topological χ_p SABS have a linear dispersion which results in a convex enhanced DOS below the gap. Interestingly, there is still a minimum at $E = 0$, stemming from graphene's band structure. Indeed, the convex enhanced DOS is suppressed around $|E| \sim 0$ in Figs. 5(b) and 5(c) for the undoped case. For the

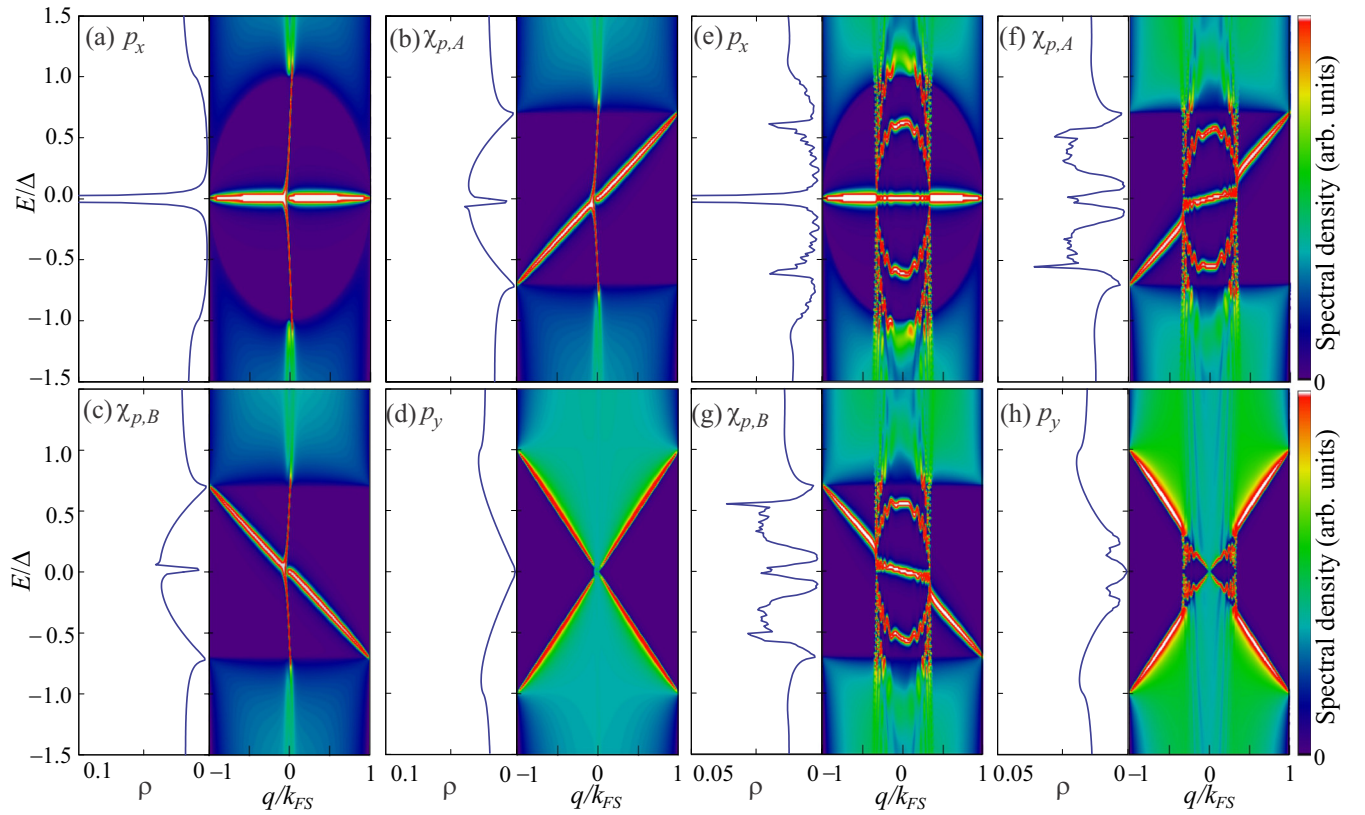


FIG. 5. Spectral density and DOS of the graphene N-G-S junction at $x = 0$. Results for different types of p -wave superconductors. The Fermi energy of the graphene layer is $E_F = 0\Delta$ in (a)–(d) and $E_F = 10\Delta$ in (e)–(h). In all cases, $E_{FN} = E_{FS} = 30\Delta$, $t_L = 0.1$, $t_R = 1$, and $d = 2\xi$.

doped situation, the linear chiral SABS have two different contributions. Outside graphene's band, it mixes with the IBS and features a linear dispersion responsible for the enhanced DOS. Close to zero energy, however, the SABS contribution to DOS mixes with that of FPR resonance that always crosses zero at $\hbar q \sim 0$. As explained at the end of Sec. III B, the sign change in $\Delta\varphi$ changes the harmonic function in Eq. (21) to a sinelike one, resulting in the emergence of a zero energy state. Additionally, the wavy FPR bands become small peaks in the DOS for subgap energies, which also happens in the

doped case. Comparing Figs. 4(e), 4(f), 4(g) and 5(e), 5(f), 5(g), we immediately observe that, for the same set of system parameters, the d -wave symmetry cases, with the notable exception of $r_1 = 0$, feature an even number of FPR bands while the number is odd for p -wave symmetry. Additionally, one of the p -wave bands is always zero at $\hbar q \sim 0$ due to the presence of nodal pairings at normal incidence like d_{xy} -wave and p_x -wave symmetries. All these signatures are the result of the rich interplay between the induced symmetries and the graphene's IBS and FPR bands, but can still be understood in the framework of the topological classification of pairing symmetries in two dimensions [85–89].

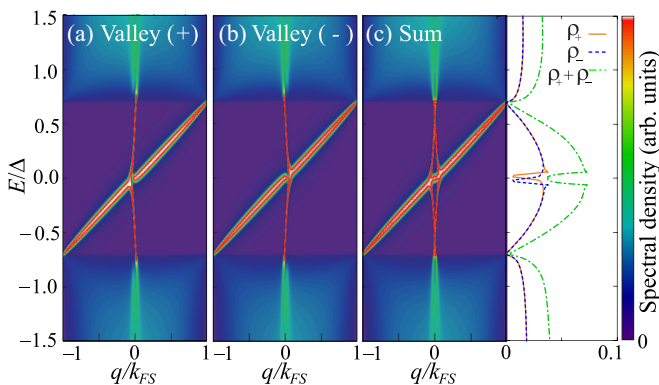


FIG. 6. Valley dependence of the spectral density and DOS of the graphene N-G-S junction at $x = 0$. All plots are calculated for the chiral p -wave symmetry.

V. DIFFERENTIAL CONDUCTANCE

We now analyze the differential conductance in the N-G-S junction sketched in Fig. 1(a). To this end, we plot Eq. (15) in Fig. 7 for d -wave (left column) and p -wave symmetries (right column). Results for s wave are similar to those of $d_{x^2-y^2}$.

We start analyzing s - and d -wave symmetries. In Fig. 7(a), we plot the conductance at $E_F = 0$ for different values of r_1 , see Fig. 1(c). In all cases, there is a strong zero-bias conductance peak (ZBCP). When $r_1 \neq 0$, we also observe two small peaks at the position of the effective superconducting gap. The ZBCP in this setup is mostly due to the contribution of graphene's ZZES at the N-G interface, where $t_L = 0.1$. However, for the case with $r_1 = 0$ where the superconductor features a nodal, flat band, the ZBCP is greatly enhanced since

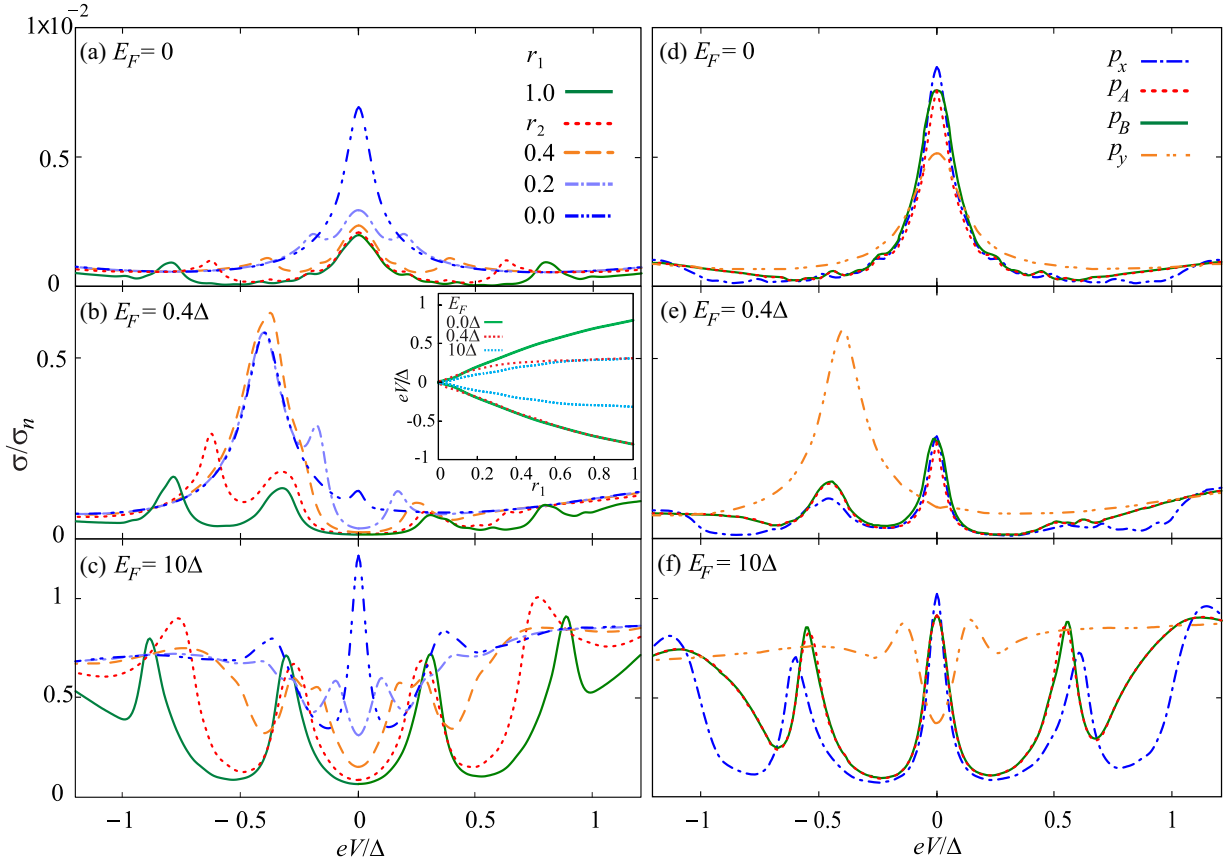


FIG. 7. Differential conductance of the graphene N-G-S junction. [(a)–(c)] Conductance for d -wave superconductors with different values of the pairing phase. The inset in (b) shows the dependence of the first resonance on r_1 for different values of the Fermi energy of the graphene stripe. [(d)–(f)] Similar results for p -wave superconductors. The Fermi energy of the graphene layer is taken at $E_F = 0$ [(a) and (d)], $E_F = 0.4\Delta$ [(b) and (e)], and $E_F = 10\Delta$ [(c) and (f)]. In all cases, $E_{FN} = E_{FS} = 30\Delta$, $t_L = 0.1$, $t_R = 1$, and $d = 2\xi$.

now merges the SABS with the ZZES. This is a signature of the gap closing and edge state for d_{xy} -wave pairing. As r_1 increases from zero, and the d_{xy} -wave mixes with the $d_{x^2-y^2}$ -wave, a fraction of this zero-energy state splits giving rise to the effective gap flatness related to the V -shaped DOS showed in cf. Fig. 4(a). We show the evolution of the split conductance peaks from finite r_1 in the inset of Fig. 7(b).

By setting $E_F \neq 0$, as it is done in Figs. 7(b) and 7(c), the ZZES moves away from zero voltage at $eV = -E_F$. In these doped cases, a ZBCP only appears for d_{xy} -wave symmetry ($r_1 = 0$). As we increase the doping of the central graphene region, the FPR become more pronounced, see Figs. 7(b) and 7(c). The main reason is that the Andreev processes at the G-S interface become retroreflections for $E_F > \Delta$, which favors the formation of closed trajectories in the G region. The geometric origin of the FPR is more clearly shown in Fig. 8, where we plot the conductance with the same parameters as in Fig. 7(c) but with $L = \xi$ (top) and $L = 3\xi$ (bottom). This is in perfect concordance with Eq. (21) where the constant energy step between Andreev levels is inversely proportional to d .

We now consider p -wave pairing symmetries. As in the previous section, we only consider p_x -, p_y -, and chiral p -wave symmetries. For the undoped graphene layer with $E_F = 0$, shown in Fig. 7(d), the conductance features a clear ZBCP. For p_y -wave pairing, the ZBCP is mostly due to the ZZES and has the smallest value because of the absence of any SABS band,

cf. Fig. 5(d). For the other symmetries, both the ZZES and the SABS contribute to the ZBCP. The highest value of the peak corresponds to p_x -wave state, where the SABS-IBS is a flat nodal surface state, as it is shown in Fig. 5(a).

Setting $E_F \neq 0$ in Figs. 7(e) and 7(f), we clearly see that the ZBCP survives for all symmetries except for the nodal p_y wave. In the strongly doped case with $E_F = 10\Delta$, the ZBCP coexists with the FPRs for the p_x - and chiral p -wave cases. Comparing Figs. 7(c) and 7(f), calculated with $L = 2\xi$, it is clear that the d -wave cases (with $r_1 \neq 0$) feature an even number of peaks, while the p_x - and chiral p -wave cases have the additional ZBCP. As was explained above, the number of resonances is determined by the length of the graphene layer as shown in Fig. 8.

It is interesting to note that the magnitude of the ZZES peak at $eV = -E_F$ in relation to the ZBCP seems to follow the opposite behavior for p - and d -wave cases, cf. Figs. 7(b) and 7(e). The ZZES peak in Fig. 7(e) is rather small for the nodal p_x - and chiral p -wave states, but has a quite pronounced contribution in the p_y -wave case, whereas the ZBCP is high for p_x and chiral p and disappear for p_y symmetry. In contrast, strong ZZES and ZBCP peaks appear when nodal d_{xy} -wave symmetry becomes dominant but gradually faded when the $d_{x^2-y^2}$ -wave contribution begins to dominate. The magnitude of the ZZES peak is completely determined by the ratio between the real and imaginary parts of the pairing as defined

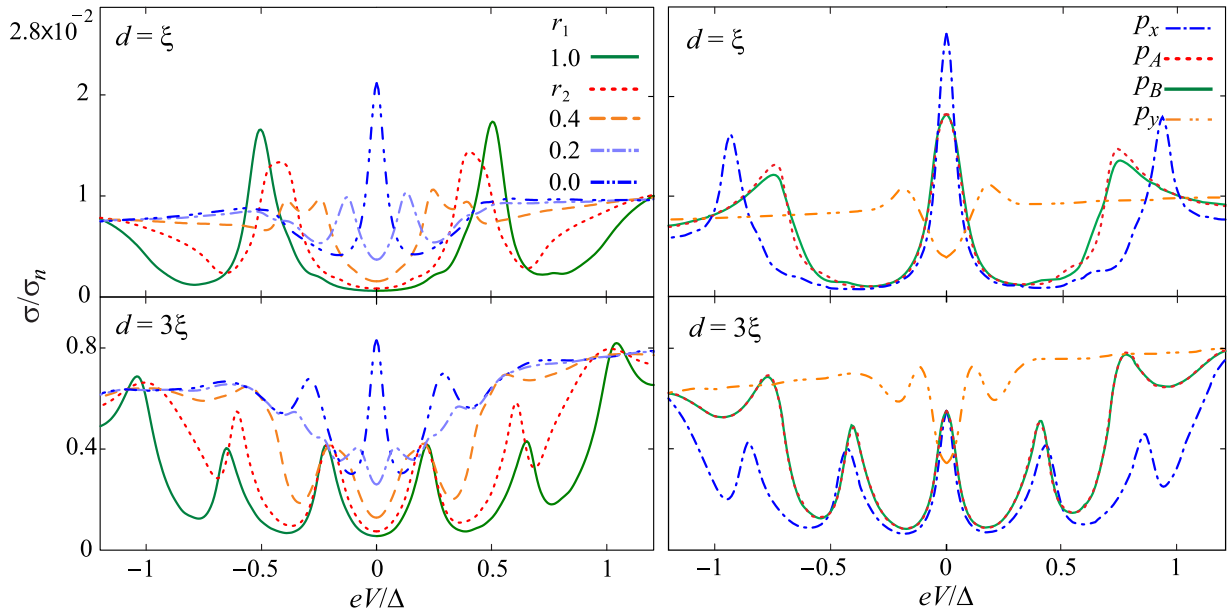


FIG. 8. Differential conductance of the graphene N-G-S junction for different widths. (Left) Conductance for d -wave superconductors with different values of the pairing phase. (Right) Similar results for p -wave superconductors. The graphene layer's width is $d = \xi$ (top) and $d = 3\xi$ (bottom). In all cases, $E_{FN} = E_{FS} = 30\Delta$, $E_F = 10\Delta$, $t_L = 0.1$, and $t_R = 1$.

in Eq. (3). For $r_1 \rightarrow 1$ (p_x and $d_{x^2-y^2}$ waves), the effective gap peaks located at $|\Delta(r_1, \theta = 0)|$ move away from $E = 0$ and momentarily merge with the ZZES to finally reach their maximum separation for $r_1 = 1$.

The dependence of the effective gap with $\hbar q$ for the different pairings is clearly observed in Figs. 4(a), 4(d) and 5(a), 5(d). The ZZES appears for values of $\hbar q$ that are close to zero for d_{xy} and p_y waves ($r_1 \rightarrow 0$) and far away from zero for $d_{x^2-y^2}$ and p_x waves ($r_1 \rightarrow 1$). After averaging over the incident modes, the ZZES thus provides a stronger contribution around $|\hbar q| \sim 0$ for pairings with $r_1 \rightarrow 0$, resulting in the strong peaks at $eV = -E_F$ in Figs. 7(b) and 7(e).

Finally, for the strongly doped case in Fig. 7(f), we clearly observe some of the characteristic behaviors of p -wave superconductors. Chiral p - and p_x -wave states feature a clear ZBCP due to the ZES bands showed in Figs. 5(f) and 5(g). The p_y -wave pairing displays a V-shape gap, with a finite minimum even though the conductance is calculated in the tunnel limit.

VI. CONCLUSION

Motivated by recent experimental advances in the implementation of graphene–superconductor ballistic junctions [46–48], we have theoretically studied the transport properties of a ballistic, finite-size graphene layer contacted by a normal and a superconducting lead. We particularly considered the emergence of unconventional superconductivity in the graphene layer [27,55].

Using a microscopic description based on Green's functions techniques, we included in our model several experimentally relevant issues like the Fabry-Pérot resonances originated by the finite length of the graphene layer, the different transmission of the graphene-reservoir interfaces, and the presence of graphene's edge states. We calculated the spectral density,

DOS and differential conductance of the graphene junction in the presence of unconventional superconductivity with different forms of d - or p -wave symmetry. We find that for energies below the effective gap, both the DOS and conductance show a very intricate profile due to the presence of several types of resonances. In addition to the Fabry-Pérot resonances and graphene's edge states, we identify the emergence of Andreev surface states and interface bound states with different dispersions. Our analytical results allows us to identify the separate contribution from each state to the DOS and their impact on the differential conductance. We thus determine the optimal conditions for the detection of unconventional superconductivity in graphene-based hybrid junctions.

In particular, we find that the presence of graphene's zigzag edge states for E_F close to zero bias can mask the emergence of a ZBCP if the superconducting pairing allows for one. A finite doping is enough to separate and distinguish the contributions from ZZES and SABS to the conductance. In the presence of high doping compared to the superconducting gap, the geometrical FPRs become stronger. However, the subgap SABS from the induced unconventional pairing still have clear signatures in the spectral density and the DOS. The SABS are responsible for the effective gap region ($|eV| < |\Delta(r_1, q = 0)|$) in the DOS, which presents a V-shape profile for p_y and d -wave symmetries with $r_1 > 0$, and a convex shape for chiral p -wave cases. On the other hand, for d_{xy} and p_x , the ZES flat band of SABS induces a strong ZBCP.

The SABS resonances do not hide the ZBCP originating from d_{xy} -, p_x -, or chiral p -wave states, for lengths of the graphene layer comparable to the superconducting coherence length. Additionally, these pairings always display an odd number of conductance resonances. Even in the presence of high doping, the FPRs mix with the SABS but the zero energy states are still present in the spectral density and result in additional zero bias peaks in the conductance.

Topological chiral SABS have distinctive signatures in the spectral density and DOS. For chiral d -wave symmetries the SABS present two co-propagating arc-shape chiral bands in the spectral density, and an enhanced DOS in the effective gap region. For chiral p -wave symmetries, the spectral density exhibits a single chiral linear band for SABS, resulting in a characteristic convex shape in the gap region of the DOS. However, since chiral SABS propagate along the interfaces, only their $q = 0$ contribution reflects in the conductance by the effective gap peaks. Therefore low doping and a wide central region are required to avoid the extra peaks of FRPs and ZZES.

Our results provide a useful guide in future experiments to study unconventional superconductivity in graphene, either induced intrinsically by the symmetry of its hexagonal lattice or by proximity effect with known superconductors.

ACKNOWLEDGMENTS

We acknowledge funding from COLCIENCIAS, Project No. 110165843163 and doctorate Scholarship 617, the European Union's Horizon 2020 research and innovation programme under the Marie Skłodowska-Curie Grant No. 743884, and Spanish MINECO through Grant No. FIS2014-55486-P and through the "María de Maeztu" Programme for Units of Excellence in R&D (MDM-2014-0377).

APPENDIX A: BOGOLIUBOV-DE GENNES-DIRAC HAMILTONIAN

We consider a semi-infinite graphene layer with a zigzag edge along the y axis at $x_L = 0$ and extending into the $x > 0$ half-plane. With this orientation the Brillouin zone has Dirac points (valleys) at $\mathbf{K}_\pm = (0, \pm K)$. The conserved momentum along the y direction is $\hbar q$. The wave function for the sublattice $A(B)$ is then given by

$$\Psi_{A(B)}(\mathbf{r}) = e^{ik_y} \Phi_{A(B)}^+(\mathbf{r}) + e^{-ik_y} \Phi_{A(B)}^-(\mathbf{r}),$$

where the functions $\Phi_{A(B)}^\pm(\mathbf{r})$ are solutions of a 2D Dirac equation

$$\begin{aligned} \hat{H}_\pm &= \hat{p}_x \sigma_x \pm q \sigma_y, \\ 0 &= (\hat{H}_\pm - (E_F + E)) \Phi^\pm(\mathbf{r}), \\ \Phi^\pm(\mathbf{r}) &= (\Phi_A^\pm(\mathbf{r}) \ \Phi_B^\pm(\mathbf{r}))^T \\ &= (f_A^\pm(x) \ f_B^\pm(x))^T e^{iqy}. \end{aligned}$$

Zigzag edges are formed by a line of atoms of only one of graphene's sublattices (A or B) and do not mix valleys. If we adopt a Dirichlet boundary condition, we get

$$\begin{aligned} \Psi_{A(B)}(\mathbf{r}) &= e^{iK_y} \Phi_{A(B)}^+(x_L, y) + e^{-iK_y} \Phi_{A(B)}^-(x_L, y) = 0, \\ \Rightarrow f_{A(B)}^\pm(x_L) &= 0. \end{aligned}$$

Then, we can consider the boundary problem separately and use only one valley. The Dirac-Bogoliubov-de Gennes (DBdG) Hamiltonian for a 2D graphene sheet adopts the form

$$H_{\text{BDG}} = \begin{pmatrix} \check{H} - \varepsilon_F \check{I} & \check{\Delta}(\mathbf{k}) \\ \check{\Delta}^\dagger(\mathbf{k}) & \varepsilon_F \check{I} - T \check{H} T^{-1} \end{pmatrix},$$

where we are considering the weak-coupling approximation (\mathbf{k} fixed on the Fermi surface) where the order parameter is only angle dependent [60], i.e.,

$$\check{\Delta}(\mathbf{k}) = \check{\Delta}(\theta),$$

and \check{H} is the single-particle Hamiltonian in sublattice and valley spaces

$$\check{H} = \begin{pmatrix} \hat{H}_+ & 0 \\ 0 & \hat{H}_- \end{pmatrix}.$$

Valley degeneracy allows us to consider only one of the two valley sets. Then, by using that $[\check{H}, T] = 0$, the 8×8 matrix decouples to a 4×4 matrix equation for zigzag edges, namely,

$$H_{\text{BDG}} = \begin{pmatrix} \hat{H}_\pm - \varepsilon_F \sigma_0 & \Delta(\mathbf{k}) \sigma_0 \\ \Delta^\dagger(\mathbf{k}) \sigma_0 & \varepsilon_F \sigma_0 - \hat{H}_\pm \end{pmatrix}. \quad (\text{A1})$$

We adopt for the pair potential the following anisotropic symmetries:

$$\begin{aligned} \Delta(\theta_\pm) &= \Delta_1 \cos(n\theta_\pm) + i\Delta_2 \sin(n\theta_\pm), \\ n = 0 &\text{ for } s \text{ wave,} \\ n = 1 &\text{ for } p \text{ wave,} \\ n = 2 &\text{ for } d \text{ wave,} \end{aligned}$$

where the parameters Δ_1 and Δ_2 obey the relations

$$\Delta_i \equiv r_i \Delta_0, \quad \sqrt{r_1^2 + r_2^2} = 1,$$

with $i = 1, 2$, and their respective phases are defined by

$$\varphi_\pm = -i \ln \left(\frac{\Delta(\theta_\pm)}{|\Delta(\theta_\pm)|} \right).$$

APPENDIX B: GREEN'S FUNCTION OF GRAPHENE LAYER WITH ZIGZAG EDGES AND INDUCED UNCONVENTIONAL SUPERCONDUCTIVITY

The solutions of the DBdG equations have the form

$$\begin{aligned} \psi_\pm^e &= e^{\pm ik_e x} (u_0 \phi_e^\pm, v_0 e^{-i\varphi_\pm} \phi_e^\pm)^T, \\ \psi_\pm^h &= e^{\pm ik_h x} (v_0 \phi_h^\pm, u_0 e^{-i\varphi_\pm} \phi_h^\pm)^T, \end{aligned}$$

with

$$\begin{aligned} \phi_{e(h)}^+ &= (1, e^{i\alpha_{e(h)}})^T, \quad \phi_{e(h)}^- = (1, -e^{-i\alpha_{e(h)}})^T, \\ \alpha_{e(h)} &= \hbar v_F \frac{k_{e(h)} + iq}{\varepsilon_F \pm E}, \quad \Omega = \sqrt{E^2 - |\Delta|^2}, \\ k_{e(h)} &= \text{sgn}(\varepsilon_F \pm \Omega) \sqrt{\frac{(\varepsilon_F \pm \Omega)^2}{\hbar^2 v_F^2} - q^2}, \\ u_0 &= \sqrt{\frac{1}{2} \left(1 + \frac{\Omega}{E} \right)}, \quad v_0 = \sqrt{\frac{1}{2} \left(1 - \frac{\Omega}{E} \right)}. \end{aligned}$$

The wave functions ψ_\pm^e propagate under a pair potential Δ , while their conjugates, $\bar{\psi}_\pm^e$, move under Δ^* . Therefore the functions $\bar{\psi}_\pm^e$ can be constructed from the solutions ψ_\pm^e by changing Δ by Δ^* and multiplying by the conjugation matrix $\hat{\sigma}_z$ (see more details in Ref. [68]). For a semi-infinite system

with one edge, the asymptotic solutions of the DBdG equations are a superposition of normal reflection and Andreev reflections as follows:

$$\begin{aligned}\psi_{<}^e &= \psi_-^e + r_e \psi_+^e + r_h \psi_-^h, \\ \psi_{<}^h &= \psi_+^h + r'_h \psi_-^h + r'_e \psi_+^e, \\ \psi_{>}^e &= \psi_+^e, \\ \psi_{>}^h &= \psi_-^h,\end{aligned}$$

where $r_{e(h)}$ are the reflection coefficients. As a boundary condition we adopted a zigzag border of atoms of sublattice B, so that the B component must be zero at $x = 0$. It then follows that

$$\begin{aligned}r_e &= e^{-2i\alpha_e} \frac{(1 - \Gamma_0^2)}{1 - \Gamma_0^2 e^{-i\Delta\varphi}} = r'_h e^{i\Delta\varphi} e^{-2i\alpha_h} e^{-2i\alpha_e}, \\ r_h &= \frac{\Gamma_0(e^{-i\Delta\varphi} - 1)}{1 - \Gamma_0^2 e^{-i\Delta\varphi}} (e^{i\alpha_h} e^{-i\alpha_e}) = r'_e, \\ \Gamma_0 &= \frac{v_0}{u_0}.\end{aligned}$$

From the asymptotic solutions that obey specific boundary conditions at the left (<) and right (>) edges of a ribbon, we construct the Green's function as [2,68,74–78]

$$\check{g}_q(x, x') = \begin{cases} \sum_{\mu, \nu} \check{C}_{\mu\nu} \psi_{<}^\mu(q, x) \bar{\psi}_{>}^{\nu T}(q, x') \check{\gamma}, & x > x' \\ \sum_{\mu, \nu} \check{C}'_{\mu\nu} \psi_{>}^\mu(q, x) \bar{\psi}_{<}^{\nu T}(q, x') \check{\gamma}, & x < x' \end{cases} \quad (\text{B1})$$

where $\mu, \nu = e, h$ label electron- and holelike solutions of the DBdG equations and we include $\check{\gamma} = \hat{t}_0 \hat{\sigma}_z$, with \hat{t}_0 the identity matrix in Nambu space, to ensure covariance [68]. By integrating Eq. (4) on the infinitesimal interval $(x' - \epsilon, x' + \epsilon)$, with $\epsilon \ll 1$, we obtain the continuity relation

$$\lim_{\epsilon \rightarrow 0} [\check{g}_q(x' + \epsilon, x') - \check{g}_q(x' - \epsilon, x')] = -\frac{i}{\hbar v_F} \hat{t}_z \hat{\sigma}_x, \quad (\text{B2})$$

with the Pauli matrix \hat{t}_z acting in Nambu space. From Eq. (B2), it is possible to determine the coefficients $\check{C}_{\mu\nu}^{(\prime)}$.

From the continuity relation, we deduce the matrix coefficients

$$\begin{aligned}\check{C}_{eh}^{(\prime)} &= 0, \\ \check{C}_{ee} &= \check{C}'_{ee} = \check{C}_{hh} = \check{C}'_{hh} = \frac{i}{\hbar v_F} \frac{1}{FH - AB} \check{Y}, \\ \check{Y} &= \begin{pmatrix} -B & 0 & H & 0 \\ 0 & -B & 0 & F e^{i\varphi_-} e^{i\varphi_+} \\ -F & 0 & A & 0 \\ 0 & -H e^{-i\varphi_+} e^{-i\varphi_-} & 0 & A \end{pmatrix}, \\ A &= \Gamma_0^2 (e^{i\alpha_h} + e^{-i\alpha_h}) - (e^{i\alpha_e} + e^{-i\alpha_e}), \\ B &= (e^{-i\alpha_h} + e^{i\alpha_h}) - \Gamma_0^2 (e^{i\alpha_e} + e^{-i\alpha_e}), \\ H &= \Gamma_0 [e^{-i\varphi_-} (e^{-i\alpha_h} - e^{-i\alpha_e}) \\ &\quad + e^{-i\varphi_+} (e^{i\alpha_h} - e^{i\alpha_e})] e^{i\varphi_-} e^{i\varphi_+}, \\ F &= \Gamma_0 [e^{-i\varphi_+} (e^{-i\alpha_h} - e^{-i\alpha_e}) \\ &\quad + e^{-i\varphi_-} (e^{i\alpha_h} - e^{i\alpha_e})].\end{aligned}$$

Thus the Green function for $x < x'$ is given by the expression

$$\begin{aligned}\check{g}_R(x, x') &= \check{C}_{ee} [\psi_-^e(x) \bar{\psi}_+^{eT}(x') + r_e \psi_+^e(x) \bar{\psi}_+^{eT}(x') \\ &\quad + r_h \psi_-^h(x) \bar{\psi}_+^{eT}(x') + \psi_+^h(x) \bar{\psi}_-^{hT}(x') \\ &\quad + r'_h \psi_-^h(x) \bar{\psi}_-^{hT}(x') + r'_e \psi_+^e(x) \bar{\psi}_-^{hT}(x')],\end{aligned}$$

where the q dependence has been omitted. A similar expression is obtained for $x > x'$ by exchanging the signs of the subindexes and changing $e, h \rightarrow h, e$ in the superindexes. For the particular case with $(x, x') = (0^+, 0)$, the Green function is given by

$$\check{g}_R = \frac{i}{\hbar v_F} \begin{pmatrix} \frac{\Psi_{31}H - B\Psi_{11}}{FH - AB} & 0 & \frac{\Psi_{33}H - B\Psi_{13}}{FH - AB} & 0 \\ -1 & 0 & 0 & 0 \\ \frac{A\Psi_{31} - F\Psi_{11}}{FH - AB} & 0 & \frac{A\Psi_{33} - F\Psi_{13}}{FH - AB} & 0 \\ 0 & 0 & 1 & 0 \end{pmatrix}, \quad (\text{B3})$$

with

$$\begin{aligned}\Psi_{11} &= 1 + \Gamma_0^2 + 2\Gamma_0 r_h + r_e (\Gamma_0^2 e^{2i\alpha_h} e^{2i\alpha_e} e^{-i\Delta\varphi} + 1), \\ \Psi_{31} &= \Gamma_0 (e^{-i\varphi_-} + e^{-i\varphi_+}) + r_h (e^{-i\varphi_-} + \Gamma_0^2 e^{-i\varphi_+}) \\ &\quad + \Gamma_0 e^{-i\varphi_+} r_e (e^{2i\alpha_h} e^{2i\alpha_e} + 1), \\ \Psi_{13} &= \Gamma_0 (e^{i\varphi_-} + e^{i\varphi_+}) + r_h (e^{i\varphi_+} + \Gamma_0^2 e^{i\varphi_-}) \\ &\quad + \Gamma_0 e^{i\varphi_-} r_e (e^{2i\alpha_h} e^{2i\alpha_e} + 1), \\ \Psi_{33} &= 1 + \Gamma_0^2 + 2\Gamma_0 r_h + r_e (e^{2i\alpha_h} e^{2i\alpha_e} + \Gamma_0^2 e^{-i\Delta\varphi}).\end{aligned}$$

Following the same procedure, the Green function of a normal graphene stripe of length d is given by

$$\check{g}_0(x, x' > x) = \frac{-i}{\hbar v_F} \begin{pmatrix} \hat{g}_e & 0 \\ 0 & \hat{g}_h \end{pmatrix},$$

with

$$\begin{aligned}\hat{g}_{e(h)} &= \frac{e^{\pm i(x'-x)k_{e(h)}}}{D_{e(h)}} \begin{pmatrix} IK & \mp s e^{\pm i\alpha} IL \\ \mp s e^{\mp i\alpha} JK & JL \end{pmatrix}_{e(h)}, \\ D_{e(h)} &= (e^{-i\alpha_{e(h)}} + e^{i\alpha_{e(h)}}) (1 + e^{\mp 2i\alpha_{e(h)}} e^{\pm 2idk_{e(h)}}), \\ I_{e(h)} &= 1 + e^{\mp 2i\alpha_{e(h)}} e^{\pm 2idk_{e(h)}} e^{\pm 2ixk_{e(h)}}, \\ J_{e(h)} &= 1 - e^{\pm 2idk_{e(h)}} e^{\pm 2ixk_{e(h)}}, \\ K_{e(h)} &= 1 - e^{\mp 2ix'k_{e(h)}}, \\ L_{e(h)} &= 1 + e^{\mp 2i\alpha_{e(h)}} e^{\mp 2ix'k_{e(h)}},\end{aligned}$$

and $s = 1$. For $x > x'$, the Green function is obtained from the transpose of the last expression by interchanging the coordinates ($x \leftrightarrow x'$) and setting $s = -1$. For a semi-infinite graphene sheet, we have $D_{e(h)} = e^{-i\alpha_{e(h)}} + e^{i\alpha_{e(h)}}$ and $F_{e(h)} = J_{e(h)} = 1$. Since Green functions for graphene with zigzag edges depend on the order of the spatial arguments, the following convention was adopted for Dyson's equation [Eq. (5)] that couples two regions with edges at $x = 0$, namely,

$$\begin{aligned}\check{G}_{ij}(x, x') &= \check{g}_{ij}(x, x') + \check{g}_{iR}(x, 0^-) \check{t}^\dagger \check{G}_{Lj}(0^+, x') \\ &= \check{g}_{ij}(x, x') + \check{g}_{iR}(x, 0^-) \check{t} \check{G}_{Rj}(0^+, x'),\end{aligned}$$

with $\check{t} = (t/2)\hat{t}_z(\hat{\sigma}_x - i\hat{\sigma}_y)$ and where 0^\pm are positive infinitesimal real numbers satisfying $0^- < 0^+$. For example, for

\check{G}_{LL} , we obtain

$$\begin{aligned}\check{G}_{LL} &= \check{g}_{LL}(\check{I} + \check{I}\check{M}_{RR}\check{g}_{RR}\check{I}^\dagger\check{g}_{LL}), \\ \check{M}_{RR} &= [\check{I} - \check{g}_{RR}\check{I}^\dagger\check{g}_{LL}\check{I}]^{-1}.\end{aligned}$$

For the model of a highly doped graphene superconductor electrode ($e^{i\alpha_e(h)} = 1$) coupled with $t = 1$ to a graphene film of length d , the last Green function has the following denominator:

$$D = (1 - e^{-i\Delta\varphi}\Gamma_0^2)^2 X, \quad (\text{B4})$$

with

$$\begin{aligned}X &= 1 + \frac{\Gamma_0^2 + e^{i\Delta\varphi/2}}{\Gamma_0^2 - e^{i\Delta\varphi/2}}(e^{-i\alpha_e}h_+ + e^{i\alpha_h}h_-) \\ &\quad + e^{-i\alpha_e}e^{i\alpha_h}h_+h_-.\end{aligned}$$

The first factor contains the SABS dispersion relation in Eq. (18), namely,

$$1 - e^{-i\Delta\varphi}\Gamma_0^2 = (E^2 - E_{SABS}^2)/\Lambda,$$

$$\Lambda = \frac{1}{2}e^{i\Delta\varphi/2}(E + \Omega)[\Omega \cos(\Delta\varphi/2) - iE \sin(\Delta\varphi/2)],$$

where Λ is responsible for some effects of superconducting phase chirality in the SABS. The factor X encodes the IBS and FPR dispersion relations [Eq. (19)],

$$\begin{aligned}X &= (E^2 - E_{IBS-FPR}^2)/\Lambda_X, \\ \Lambda_X &= \frac{E(\Phi - 1) - (1 + \Phi)\Omega}{(e^{-i\alpha_e}h_+ + e^{i\alpha_h}h_-)(1 - Z^2)} \\ &\quad \times \frac{E[C(\Phi - 1) + (1 + \Phi)] - \Omega[(1 - \Phi) - C(1 + \Phi)]}{(C(\Phi - 1) + (1 + \Phi))^2},\end{aligned}$$

with $\Phi = e^{-i\Delta\varphi}$. Here Λ_X also includes some effects of valley and superconducting phase chirality.

-
- [1] M. Sigrist and K. Ueda, Phenomenological theory of unconventional superconductivity, *Rev. Mod. Phys.* **63**, 239 (1991).
- [2] S. Kashiwaya and Y. Tanaka, Tunnelling effects on surface bound states in unconventional superconductors, *Rep. Prog. Phys.* **63**, 1641 (2000).
- [3] P. A. Lee, N. Nagaosa, and X.-G. Wen, Doping a mott insulator: Physics of high-temperature superconductivity, *Rev. Mod. Phys.* **78**, 17 (2006).
- [4] A. P. Mackenzie and Y. Maeno, The superconductivity of Sr_2RuO_4 and the physics of spin-triplet pairing, *Rev. Mod. Phys.* **75**, 657 (2003); Y. Maeno, S. Kittaka, T. Nomura, S. Yonezawa, and K. Ishida, Evaluation of spin-triplet superconductivity in Sr_2RuO_4 , *J. Phys. Soc. Jpn.* **81**, 011009 (2012); C. Kallin, Chiral p-wave order in Sr_2RuO_4 , *Rep. Prog. Phys.* **75**, 042501 (2012).
- [5] N. Read and D. Green, Paired states of fermions in two dimensions with breaking of parity and time-reversal symmetries and the fractional quantum Hall effect, *Phys. Rev. B* **61**, 10267 (2000).
- [6] D. A. Ivanov, Non-Abelian Statistics of Half-Quantum Vortices in p-Wave Superconductors, *Phys. Rev. Lett.* **86**, 268 (2001).
- [7] J. Alicea, New directions in the pursuit of majorana fermions in solid state systems, *Rep. Prog. Phys.* **75**, 076501 (2012); C. W. J. Beenakker, Search for majorana fermions in superconductors, *Annu. Rev. Condens. Matter Phys.* **4**, 113 (2013); S. Das Sarma, M. Freedman, and C. Nayak, Majorana zero modes and topological quantum computation, *Npj Quant. Info.* **1**, 15001 (2015).
- [8] R. M. Lutchyn, J. D. Sau, and S. Das Sarma, Majorana Fermions and a Topological Phase Transition in Semiconductor-Superconductor Heterostructures, *Phys. Rev. Lett.* **105**, 077001 (2010).
- [9] Y. Oreg, G. Refael, and F. von Oppen, Helical Liquids and Majorana Bound States in Quantum Wires, *Phys. Rev. Lett.* **105**, 177002 (2010).
- [10] A. C. Potter and P. A. Lee, Multichannel Generalization of Kitaev's Majorana End States and a Practical Route to Realize them in Thin Films, *Phys. Rev. Lett.* **105**, 227003 (2010); Engineering a $p + ip$ superconductor: Comparison of topological insulator and rashba spin-orbit-coupled materials, *Phys. Rev. B* **83**, 184520 (2011).
- [11] G. E. Volovik, *Universe in a Helium Droplet* (Oxford University Press, Oxford UK, 2003).
- [12] A. P. Schnyder and P. M. R. Brydon, Topological surface states in nodal superconductors, *J. Phys.: Condens. Matter* **27**, 243201 (2015).
- [13] C. Kallin and J. Berlinsky, Chiral superconductors, *Rep. Prog. Phys.* **79**, 054502 (2016).
- [14] M. Fogelström, D. Rainer, and J. A. Sauls, Tunneling into Current-Carrying Surface States of High- T_c Superconductors, *Phys. Rev. Lett.* **79**, 281 (1997).
- [15] G. E. Volovik, On edge states in superconductors with time inversion symmetry breaking, *J. Exp. Theor. Phys. Lett.* **66**, 522 (1997).
- [16] R. B. Laughlin, Magnetic Induction of $d_{x^2-y^2} + id_{xy}$ Order in High- T_c Superconductors, *Phys. Rev. Lett.* **80**, 5188 (1998).
- [17] N. B. Kopnin and M. M. Salomaa, Mutual friction in superfluid ^3He : Effects of bound states in the vortex core, *Phys. Rev. B* **44**, 9667 (1991).
- [18] T. Senthil, J. B. Marston, and M. P. A. Fisher, Spin quantum Hall effect in unconventional superconductors, *Phys. Rev. B* **60**, 4245 (1999).
- [19] B. Horovitz and A. Golub, Superconductors with broken time-reversal symmetry: Spontaneous magnetization and quantum Hall effects, *Phys. Rev. B* **68**, 214503 (2003).
- [20] D. Asahi and N. Nagaosa, Topological indices, defects, and majorana fermions in chiral superconductors, *Phys. Rev. B* **86**, 100504(R) (2012).
- [21] S.-J. Sun, C.-H. Chung, Y.-Y. Chang, W.-F. Tsai, and F.-C. Zhang, Helical majorana fermions in $d_{x^2-y^2} + id_{xy}$ -wave topological superconductivity of doped correlated quantum spin Hall insulators, *Sci. Rep.* **6**, 24102 (2016).
- [22] Y. Jiang, D.-X. Yao, E. W. Carlson, H.-D. Chen, and JiangPing Hu, Andreev conductance in the $d + id'$ -wave superconducting states of graphene, *Phys. Rev. B* **77**, 235420 (2008).

- [23] A. M. Black-Schaffer, Edge Properties and Majorana Fermions in the Proposed Chiral d -Wave Superconducting State of Doped Graphene, *Phys. Rev. Lett.* **109**, 197001 (2012).
- [24] A. M. Black-Schaffer and C. Honerkamp, Chiral d -wave superconductivity in doped graphene, *J. Phys.: Condens. Matter* **26**, 423201 (2014).
- [25] R. Nandkishore, L. S. Levitov, and A. V. Chubukov, Chiral superconductivity from repulsive interactions in doped graphene, *Nat. Phys.* **8**, 158 (2012).
- [26] B. Uchoa and A. H. Castro Neto, Superconducting States of Pure and Doped Graphene, *Phys. Rev. Lett.* **98**, 146801 (2007).
- [27] A. Di Bernardo, O. Millo, M. Barbone, H. Alpern, Y. Kalcheim, U. Sassi, A. K. Ott, D. De Fazio, D. Yoon, M. Amado, A. C. Ferrari, J. Linder, and J. W. A. Robinson, p -wave triggered superconductivity in single-layer graphene on an electron-doped oxide superconductor, *Nat. Commun.* **8**, 14024 (2017).
- [28] G. E. Blonder, M. Tinkham, and T. M. Klapwijk, Transition from metallic to tunneling regimes in superconducting microconstrictions: Excess current, charge imbalance, and supercurrent conversion, *Phys. Rev. B* **25**, 4515 (1982).
- [29] T. Klapwijk and S. Ryabchun, Direct observation of ballistic Andreev reflection, *J. Exp. Theor. Phys.* **119**, 997 (2014).
- [30] Y. Tanaka and S. Kashiwaya, Theory of Tunneling Spectroscopy of d -Wave Superconductors, *Phys. Rev. Lett.* **74**, 3451 (1995).
- [31] S. Kashiwaya, Y. Tanaka, M. Koyanagi, H. Takashima, and K. Kajimura, Origin of zero-bias conductance peaks in high- t_c superconductors, *Phys. Rev. B* **51**, 1350 (1995).
- [32] S. Kashiwaya, Y. Tanaka, M. Koyanagi, and K. Kajimura, Theory for tunneling spectroscopy of anisotropic superconductors, *Phys. Rev. B* **53**, 2667 (1996).
- [33] C. Honerkamp and M. Sigrist, Andreev reflection in unitary and non-unitary triplet states, *J. Low Temp. Phys.* **111**, 895 (1998).
- [34] B. Lu, P. Buset, Y. Tanuma, A. A. Golubov, Y. Asano, and Y. Tanaka, Influence of the impurity scattering on charge transport in unconventional superconductor junctions, *Phys. Rev. B* **94**, 014504 (2016).
- [35] P. Buset, B. Lu, S. Tamura, and Y. Tanaka, Current fluctuations in unconventional superconductor junctions with impurity scattering, *Phys. Rev. B* **95**, 224502 (2017).
- [36] J. Wiedenmann, E. Liebhaber, J. Kübert, E. Bocquillon, P. Buset, C. Ames, H. Buhmann, T. M. Klapwijk, and L. W. Molenkamp, Transport spectroscopy of induced superconductivity in the three-dimensional topological insulator HgTe, *Phys. Rev. B* **96**, 165302 (2017).
- [37] W. Liang, M. Bockrath, D. Bozovic, J. H. Hafner, M. Tinkham, and H. Park, Fabry - perot interference in a nanotube electron waveguide, *Nature* **411**, 665 (2001).
- [38] A. V. Kretinin, R. Popovitz-Biro, D. Mahalu, and H. Shtrikman, Multimode Fabry-pérot conductance oscillations in suspended stacking-faults-free InAs nanowires, *Nano Lett.* **10**, 3439 (2010).
- [39] S. Das Sarma, S. Adam, E. H. Hwang, and E. Rossi, Electronic transport in two-dimensional graphene, *Rev. Mod. Phys.* **83**, 407 (2011).
- [40] A. V. Rozhkov, G. Giavaras, Y. P. Bliokh, V. Freilikher, and F. Nori, Electronic properties of mesoscopic graphene structures: Charge confinement and control of spin and charge transport, *Phys. Rep.* **503**, 77 (2011).
- [41] T. O. Wehling, A. M. Black-Schaffer, and A. V. Balatsky, Dirac materials, *Adv. Phys.* **63**, 1 (2014).
- [42] F. Xia, V. Perebeinos, Y.-M. Lin, Y. Wu, and P. Avouris, The origins and limits of metal-graphene junction resistance, *Nat. Nano* **6**, 179 (2011); Y. Wu, V. Perebeinos, Y.-M. Lin, T. Low, F. Xia, and P. Avouris, Quantum behavior of graphene transistors near the scaling limit, *Nano Lett.* **12**, 1417 (2012).
- [43] R. Drost, A. Uppstu, F. Schulz, S. K. Hämäläinen, M. Ervasti, A. Harju, and P. Liljeroth, Electronic states at the graphene-hexagonal boron nitride zigzag interface, *Nano Lett.* **14**, 5128 (2014); R. Drost, S. Kezilebieke, M. M. Ervasti, S. K. Hämäläinen, F. Schulz, A. Harju, and P. Liljeroth, Synthesis of extended atomically perfect zigzag graphene - boron nitride interfaces, *Sci. Rep.* **5**, 16741 (2015).
- [44] H. B. Heersche, P. Jarillo-Herrero, J. B. Oostinga, L. M. K. Vandersypen, and A. F. Morpurgo, Bipolar supercurrent in graphene, *Nature (London)* **446**, 56 (2007); F. Miao, S. Wijeratne, Y. Zhang, U. C. Coskun, W. Bao, and C. N. Lau, Phase-coherent transport in graphene quantum billiards, *Science* **317**, 1530 (2007); A. Shailos, W. Nativel, A. Kasumov, C. Collet, M. Ferrier, S. Guéron, R. Deblock, and H. Bouchiat, Proximity effect and multiple Andreev reflections in few-layer graphene, *Europhys. Lett.* **79**, 57008 (2007); X. Du, I. Skachko, and E. Y. Andrei, Josephson current and multiple Andreev reflections in graphene SNS junctions, *Phys. Rev. B* **77**, 184507 (2008).
- [45] P. Rickhaus, M. Weiss, L. Marot, and C. Schönenberger, Quantum Hall effect in graphene with superconducting electrodes, *Nano Lett.* **12**, 1942 (2012).
- [46] V. E. Calado, S. Goswami, G. Nanda, M. Diez, A. R. Akhmerov, K. Watanabe, T. Taniguchi, T. M. Klapwijk, and L. M. K. Vandersypen, Ballistic Josephson junctions in edge-contacted graphene, *Nat. Nano* **10**, 761 (2015).
- [47] M. Ben Shalom, M. J. Zhu, V. I. Falko, A. Mishchenko, A. V. Kretinin, K. S. Novoselov, C. R. Woods, K. Watanabe, T. Taniguchi, A. K. Geim, and J. R. Prance, Quantum oscillations of the critical current and high-field superconducting proximity in ballistic graphene, *Nat. Phys.* **12**, 318 (2016).
- [48] D. K. Efetov, L. Wang, C. Handschin, K. B. Efetov, J. Shuang, R. Cava, T. Taniguchi, K. Watanabe, J. Hone, C. R. Dean, and P. Kim, Specular interband Andreev reflections at van der Waals interfaces between graphene and NbSe₂, *Nat. Phys.* **12**, 328 (2016).
- [49] C. W. J. Beenakker, Specular Andreev Reflection in Graphene, *Phys. Rev. Lett.* **97**, 067007 (2006).
- [50] T. Dirks, T. L. Hughes, S. Lal, B. Uchoa, Y.-F. Chen, C. Chialvo, P. M. Goldbart, and N. Mason, Transport through Andreev bound states in a graphene quantum dot, *Nat. Phys.* **7**, 386 (2011).
- [51] Z. B. Tan, D. Cox, T. Nieminen, P. Lähteenmäki, D. Golubev, G. B. Lesovik, and P. J. Hakonen, Cooper Pair Splitting by Means of Graphene Quantum Dots, *Phys. Rev. Lett.* **114**, 096602 (2015).
- [52] C. Tonnoir, A. Kimouche, J. Coraux, L. Magaud, B. Delsol, B. Gilles, and C. Chapelier, Induced Superconductivity in Graphene Grown on Rhenium, *Phys. Rev. Lett.* **111**, 246805 (2013).
- [53] B. M. Ludbrook, G. Levy, P. Nigge, M. Zonno, M. Schneider, D. J. Dvorak, C. N. Veenstra, S. Zhdanovich, D. Wong, P. Dosanjh, C. Straßer, A. Stöhr, S. Forti, C. R. Ast, U. Starke, and

- A. Damascelli, Evidence for superconductivity in li-decorated monolayer graphene, *Proc. Natl. Acad. Sci. USA* **112**, 11795 (2015).
- [54] J. Chapman, Y. Su, C. A. Howard, D. Kundys, A. N. Grigorenko, F. Guinea, A. K. Geim, I. V. Grigorieva, and R. R. Nair, Superconductivity in ca-doped graphene laminates, *Sci. Rep.* **6**, 23254 (2016).
- [55] Y. Cao, V. Fatemi, S. Fang, K. Watanabe, T. Taniguchi, E. Kaxiras, and P. Jarillo-Herrero, Unconventional superconductivity in magic-angle graphene superlattices, *Nature* **556**, 43 (2018).
- [56] S. Bhattacharjee and K. Sengupta, Tunneling Conductance of Graphene Nis Junctions, *Phys. Rev. Lett.* **97**, 217001 (2006).
- [57] A. R. Akhmerov and C. W. J. Beenakker, Pseudodiffusive conduction at the dirac point of a normal-superconductor junction in graphene, *Phys. Rev. B* **75**, 045426 (2007).
- [58] G. Tkachov, Fine structure of the local pseudogap and fano effect for superconducting electrons near a zigzag graphene edge, *Phys. Rev. B* **76**, 235409 (2007).
- [59] J. Linder and A. Sudbø, Dirac Fermions and Conductance Oscillations in *s*- and *d*-Wave Superconductor-Graphene Junctions, *Phys. Rev. Lett.* **99**, 147001 (2007).
- [60] J. Linder and A. Sudbø, Tunneling conductance in *s*- and *d*-wave superconductor-graphene junctions: Extended blonder-tinkham-klapwijk formalism, *Phys. Rev. B* **77**, 064507 (2008).
- [61] P. Buset, A. L. Yeyati, and A. Martín-Rodero, Microscopic theory of the proximity effect in superconductor-graphene nanostructures, *Phys. Rev. B* **77**, 205425 (2008).
- [62] A. M. Black-Schaffer and S. Doniach, Self-consistent solution for proximity effect and josephson current in ballistic graphene sns josephson junctions, *Phys. Rev. B* **78**, 024504 (2008).
- [63] P. Buset, W. Herrera, and A. Levy Yeyati, Proximity-induced interface bound states in superconductor-graphene junctions, *Phys. Rev. B* **80**, 041402(R) (2009).
- [64] Q. feng Sun and X. C. Xie, Quantum transport through a graphene nanoribbon-superconductor junction, *J. Phys.: Condens. Matter* **21**, 344204 (2009).
- [65] S. Gómez, P. Buset, W. J. Herrera, and A. Levy Yeyati, Selective focusing of electrons and holes in a graphene-based superconducting lens, *Phys. Rev. B* **85**, 115411 (2012).
- [66] C. W. J. Beenakker, Colloquium, *Rev. Mod. Phys.* **80**, 1337 (2008).
- [67] J. Linder, A. M. Black-Schaffer, T. Yokoyama, S. Doniach, and A. Sudbø, Josephson current in graphene: Role of unconventional pairing symmetries, *Phys. Rev. B* **80**, 094522 (2009).
- [68] W. J. Herrera, P. Buset, and A. L. Yeyati, A green function approach to graphene-superconductor junctions with well-defined edges, *J. Phys.: Condens. Matter* **22**, 275304 (2010).
- [69] P. Buset, W. Herrera, and A. Levy Yeyati, Formation of interface bound states on a graphene-superconductor junction in the presence of charge inhomogeneities, *Graphene* **2**, 7 (2013).
- [70] P. Buset, F. Keidel, Y. Tanaka, N. Nagaosa, and B. Trauzettel, Transport signatures of superconducting hybrids with mixed singlet and chiral triplet states, *Phys. Rev. B* **90**, 085438 (2014).
- [71] A. M. Black-Schaffer and S. Doniach, Resonating valence bonds and mean-field *d*-wave superconductivity in graphite, *Phys. Rev. B* **75**, 134512 (2007).
- [72] B. Lu, P. Buset, K. Yada, and Y. Tanaka, Tunneling spectroscopy and josephson current of superconductor-ferromagnet hybrids on the surface of a 3D TI, *Supercond. Sci. Technol.* **28**, 105001 (2015).
- [73] Y. Tanaka, M. Sato, and N. Nagaosa, Symmetry and topology in superconductors —odd-frequency pairing and edge states—, *J. Phys. Soc. Jpn.* **81**, 011013 (2012).
- [74] W. L. McMillan, Theory of superconductor-normal metal interfaces, *Phys. Rev.* **175**, 559 (1968).
- [75] A. Furusaki and M. Tsukada, Dc josephson effect and Andreev reflection, *Solid State Commun.* **78**, 299 (1991).
- [76] P. Buset, B. Lu, G. Tkachov, Y. Tanaka, E. M. Hankiewicz, and B. Trauzettel, Superconducting proximity effect in three-dimensional topological insulators in the presence of a magnetic field, *Phys. Rev. B* **92**, 205424 (2015).
- [77] F. Crépin, P. Buset, and B. Trauzettel, Odd-frequency triplet superconductivity at the helical edge of a topological insulator, *Phys. Rev. B* **92**, 100507(R) (2015).
- [78] D. Breunig, P. Buset, and B. Trauzettel, Creation of Spin-Triplet Cooper Pairs in the Absence of Magnetic Ordering, *Phys. Rev. Lett.* **120**, 037701 (2018).
- [79] S. Gomez, Transporte eléctrico en superconductores no convencionales, (2011) www.bdigital.unal.edu.co/8020/.
- [80] J. C. Cuevas, A. Martín-Rodero, and A. L. Yeyati, Hamiltonian approach to the transport properties of superconducting quantum point contacts, *Phys. Rev. B* **54**, 7366 (1996).
- [81] T. Löfwander, V. S. Shumeiko, and G. Wendin, Andreev bound states in high- T_c superconducting junctions, *Supercond. Sci. Technol.* **14**, R53 (2001).
- [82] L. Brey and H. A. Fertig, Electronic states of graphene nanoribbons studied with the dirac equation, *Phys. Rev. B* **73**, 235411 (2006).
- [83] G. Tkachov, Dirac fermion quantization on graphene edges: Isospin-orbit coupling, zero modes, and spontaneous valley polarization, *Phys. Rev. B* **79**, 045429 (2009).
- [84] G. Tkachov and M. Hentschel, Coupling between chirality and pseudospin of dirac fermions: Non-analytical particle-hole asymmetry and a proposal for a tunneling device, *Phys. Rev. B* **79**, 195422 (2009).
- [85] M. Sato, Topological properties of spin-triplet superconductors and fermi surface topology in the normal state, *Phys. Rev. B* **79**, 214526 (2009).
- [86] M. Sato, Topological odd-parity superconductors, *Phys. Rev. B* **81**, 220504(R) (2010).
- [87] S. Ryu, A. P. Schnyder, A. Furusaki, and A. W. W. Ludwig, Topological insulators and superconductors: tenfold way and dimensional hierarchy, *New J. Phys.* **12**, 065010 (2010).
- [88] J. C. Budich and B. Trauzettel, From the adiabatic theorem of quantum mechanics to topological states of matter, *Phys. Status Solidi (RRL)* **7**, 109 (2013).
- [89] S. Kashiwaya, H. Kashiwaya, K. Saitoh, Y. Mawatari, and Y. Tanaka, Tunneling spectroscopy of topological superconductors, *Physica E (Amsterdam)* **55**, 25 (2014).